Theory of Spin Waves in Rare Earth Metals with Non-Linear c-f Exchange Interaction Effect

Keimei Kaino[1*] and Tadao Kasuya[2]

[1]*Emeritus Professor, National Institute of Technology, Sendai College, Sendai 989-3128, Japan*
[2]*Emeritus Professor, Faculty of Science, Tohoku University, Japan*
[*]*E-mail address: kaino@sendai-nct.ac.jp*

(Received April 26, 2017; Accepted July 25, 2017)

Using a simple band model which produces a helical spin ordering, we show the magnetic phase diagram by minimizing the unperturbed energy which includes the c-f exchange interaction by replacing the f-spin operator $\boldsymbol{S}_n$ with the expectation value $\langle \boldsymbol{S}_n \rangle$. As the c-f exchange interaction increases, the helix and the cone structures appears without any crystal fields, and then the ferromagnetic structure becomes more stable. Secondly, we obtain formulae of spin-wave dispersions and show their instabilities on the second-order transition boundaries. Near the ferro-helix boundary, the spin-wave constant of the ferromagnetic spin-wave vanishes, while in the helical phase the whole region of the wave-number $0 < q_z < Q$ shows softening where the helical wave-number Q decreases continuously. Thirdly, by the method of the double-time Green function, we derive the spin-wave dispersion at finite temperatures. Finally, anomalous properties in magnon dispersions at finite temperatures for Gd, Ho and those for diluted Tb-Y alloys are explained by use of numerical calculations.

Key words: c-f Exchange Interaction, Magnon Instabilities, Rare Earth Metals, Spin-Wave Dispersions

1. Introduction

Rare-earth metals are most typical materials to which the c-f exchange interaction model is applicable, where c means the conduction electron [1]. In heavy rare-earth metals the fascinating variety of equilibrium magnetic configurations has been found by neutron diffraction [2]. For each of the heavy rare-earth metals except ferromagnetic Gd, there are at least two temperature regions of magnetic order. There is observed a transition at a temperature T_N to a helical or linear oscillatory configuration. At lower temperatures, T_C, further transitions to ferromagnetic, conical, or antiphase domain-type configurations are observed.

By the assumption that Fermi energy is much greater than the c-f exchange energy, the c-f exchange interaction is treated by the second-order perturbation and hence the Heisenberg-type f-f exchange interaction is derived. Usual treatment of spin-waves in rare-earth metals has been based on the Heisenberg exchange interaction including crystalline anisotropy and magnetostriction [3,4,5].

In the ferromagnetic structure, the spin-wave spectrum for the isotropic Heisenberg-type spin system has the formula

$$\hbar\omega(\boldsymbol{q}) = 2J[J(\boldsymbol{0}) - J(\boldsymbol{q})] \tag{1}$$

where J is the total angular momentum and $J(\boldsymbol{q})$ is the Fourier-transformed exchanged interaction constant between local spins. In the second-order perturbation of the c-f exchange interaction, $J(\boldsymbol{q})$ can be readily evaluated. Its $\boldsymbol{q}$-dependence comes from the band structure as well as the $\boldsymbol{q}$-dependence of the c-f exchange matrix element [1]. By use of the band structure calculated by Keeton and Loucks [6] and a phenomenological $\boldsymbol{q}$-dependent matrix element of a Gaussian form, Evenson and Liu [7] and Liu *et al*. [8] obtained a magnon spectrum of Gd in the c-direction. By using the APW band calculation, Lindgård *et al*. [9] made an ab initio calculation of $J(\boldsymbol{q})$ for Gd for $\boldsymbol{q}$ along the c-axis and showed that the calculated $J(\boldsymbol{q})$ is in good overall agreement with experimental one [10], provided that a uniform scale factor is multiplied. Nonetheless, there remains a large discrepancy at small values of $\boldsymbol{q}$.

Those calculated bands are for the paramagnetic state. The relativistic APW band calculation for heavy rare-earth metal [6] showed that the 'webbing' between two arms near L of those Fermi surfaces exists for Lu, Er and Dy, as well as Y and determines the helical wavevector $\boldsymbol{Q}$. The webbing, however, is nearly absent in Gd. Measurement of the de Haas-van Alphen effect in Y by Mattocks and Young [11] confirmed that the general shape of the band-structure is as predicted by the above RAPW calculation.

In the case of Gd, for example, a ferromagnetic structure is observed below $T_C = 293$ K with a total magnetic moment of 7.63 μ_B pre atom in zero field, where 0.63 μ_B per atom is due to the polarization of the c electron [12]. Harmon and Freeman [13] investigated the ferromagnetic band-structure of Gd using the spin-polarized APW method and estimated that an average exchange splittings of 0.81(0.57) eV near the Fermi level induces the excess moment of 0.72(0.55) μ_B per atom. Hence the average c-f exchange constant I is estimated to be about 0.097 eV in Gd, where the c-f exchange interaction is defined as $I(\boldsymbol{S}\cdot\boldsymbol{\sigma})$ in which $\boldsymbol{S}$ is the f spin-operator and $\boldsymbol{\sigma}$ the Pauli spin-

doi:10.5047/forma.2017.sii005

operator of the c electron. The effective Fermi energy for the flat surfaces mentioned above is estimated to be about 0.2 eV in the paramagnetic Dy [6]. Hence this energy is rather smaller than the c-f exchange energy.

When the temperature is lowered, spin-wave dispersions in Ho [14] and $Tb_{0.9}Ho_{0.1}$ [15] increase for wavenumber q larger than the helical wavenumber Q but decrease for q smaller than Q. This feature is opposite to the temperature dependence derived from the simple Heisenberg model. In rare earth metals except Gd, the anisotropy energy and the magneto-elastic effects modify the magnon spectrum [3,16]. With lowering temperature, the anisotropy energy increases and causes an increase in the magnitude of magnon energies in a similar way to ferromagnetic Tb and Dy [17].

At low temperatures, all alloys of Gd, Tb, Dy and Ho diluted with yttrium exhibit helical structures. Wakabayashi and Nicklow [14,18,19] showed in these alloys of Tb and Ho diluted with Y that well-defined helical spin waves exist and that when the concentrations of magnetic ions decrease, the magnon velocities at $q = 0$ become larger, while the magnon energies for $q > Q$ become lower and flatter.

Hence spin-wave dispersions in heavy rare-earth metals show various anomalous features which are not explained by the simple Heisenberg exchange interaction model [5]. Prominent features that we treat in this paper are the following.

(a) In Gd, the ferromagnetic magnon dispersion is normal at low temperature but shows an anomalous dispersion near T_c, that is, an initial flat dispersion followed by a sharp increase at a critical wavenumber $q = Q_c$ [10] which is nearly equal to the initial helical wavenumber in Tb and Dy.

(b) When the temperature is lowered, magnon dispersions of the helical structure in Ho [14] and $Tb_{0.9}Ho_{0.1}$ [15] increase for wavenumber q larger than the helical wavenumber Q but decrease for q smaller than Q.

(c) The alloys Tb_xY_{1-x} ($0.05 < x < 0.85$) have helical structure. As the value of x decreases, the magnon energies decrease for $q > Q$ but increase for $q < Q$ [19].

The feature (a) concerning the temperature dependence of spin-wave dispersion is opposite to the simple Heisenberg system, because any sharp structure is smeared out by approaching T_C. The non-linear c-f exchange effect is shown to be most important for both the thermal variation of the helical Q and the magnetic phase diagram [20]. Hence we expect that the non-linear effect plays also an important role on the magnon dispersions at small q values and their temperature dependence [21,22] because the ferromagnetic state in Gd passes through near the ferro-cone or ferro-helix boundary near T_C (see Fig. 13) [20].

Concerning the feature (b), this anomaly is also related with the non-linear c-f exchange interaction effect. As shown later, when $\langle S \rangle$ increases with decreasing temperature, the helix approaches the helix-ferro boundary (see Fig. 3), where the magnon dispersion in the helix shows softening for small q values.

When the concentration of magnetic ions decreases, the average magnetic moment $\langle S \rangle$ at each site decreases on the standpoint of the mean lattice approximation. Therefore the decrease of the concentration corresponds to the increase of the temperature. We expect to explain not only the feature (b) but also the feature (c) from the same viewpoint of the non-linear c-f exchange effect.

The organization of this paper is the following. After summarizing the formulation in Sec. 2, we show the magnetic phase diagram. In Sec. 3, the spin-wave dispersion of ferromagnet and its softening on the magnetic phase boundaries are discussed. In Sec. 4, the spin-wave dispersions of conical and helical structures are discussed. Here and in Appendix C, magnon softening and continuity of magnon dispersions at the phase boundaries are investigated. In Sec. 5, we discuss an application of our calculation to finite temperatures. The final section is devoted to comparison of the calculation with experiments. It is noted that this paper is written based on our research report [23].

2. Model Hamiltonian and Magnetic Phase Diagram at $T = 0$

2.1 Model hamiltonian and formulation

The model Hamiltonian consists of the band energy term and the c-f exchange term. As shown by Harmon and Freeman [24], the c-f exchange matrix element $I(\boldsymbol{k}, \boldsymbol{k}')$ is a complicated function of $\boldsymbol{k}$ and $\boldsymbol{k}'$. In the following, we replace $I(\boldsymbol{k}, \boldsymbol{k}')$ with a constant and adjustable parameter I.

$$H = \sum_{\boldsymbol{k}\sigma} \varepsilon_{\boldsymbol{k}} a^{\dagger}_{\boldsymbol{k}\sigma} a_{\boldsymbol{k}\sigma} - IN^{-1} \sum_{\boldsymbol{k}\alpha} \sum_{\boldsymbol{k}'\beta} \times \sum_{n} e^{i(\boldsymbol{k}-\boldsymbol{k}')\cdot \boldsymbol{R}_n} a^{\dagger}_{\boldsymbol{k}\alpha} (\boldsymbol{\sigma} \cdot \boldsymbol{S}_n)_{\alpha\beta} a_{\boldsymbol{k}'\beta} \qquad (2)$$

where S denotes the total angular momentum and the unit $\hbar = k_B = 1$ are employed.

The band model $\varepsilon_{\boldsymbol{k}}$ has a pair of flat, parallel Fermi surfaces perpendicular to the k_z-axis [6]. We linearize the spectrum $\varepsilon_{\boldsymbol{k}}$ in the k_z-direction around the Fermi level [25] and furthermore the spectrum perpendicular to its direction.

$$\varepsilon_{\boldsymbol{k}} = v_1 |k_z| + v_2 (k_\perp - k_a)\, \Theta(k_\perp - k_a) \qquad (3)$$

where the velocities v_1 and v_2 are parallel and perpendicular to the k_z axis, respectively, and $k_\perp = |k_x| + |k_y|$. The step function $\Theta(k)$ is defined as $\Theta(k) = 0$ for $k < 0$ and $\Theta(k) = 1$ for $k > 0$. As k_a increases, the flat part of the Fermi surfaces increase as shown in Fig. 1. The real Fermi surfaces have ripples [6] and are smeared by the temperature and life time broadening effects. They are taken into account by an effect of a simple life time $i\gamma$ in the conduction electrons. This approximation is too simple to compare calculated results with experimental results in rare earth metals, but semi-qualitative comparison is possible [20].

To treat the nonlinear effect of the c-f exchange interaction, each f-spin operator is rewritten as

$$\boldsymbol{S}_n = \langle \boldsymbol{S}_n \rangle + (\boldsymbol{S}_n - \langle \boldsymbol{S}_n \rangle), \qquad (4)$$

where $\langle A \rangle$ means the expectation value of A, and the first term is included in the unperturbed Hamiltonian H_0. The ordered structure $\langle \boldsymbol{S}_n \rangle$ is assumed to be a cone structure

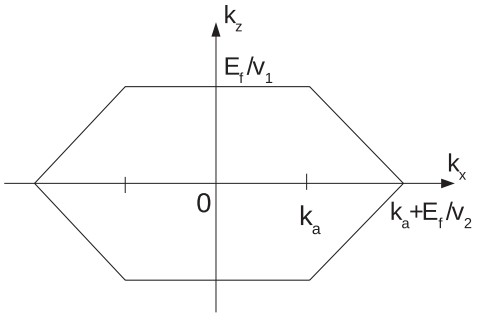

Fig. 1. Conduction band model $\varepsilon_{\boldsymbol{k}}$ for $k_y = 0$.

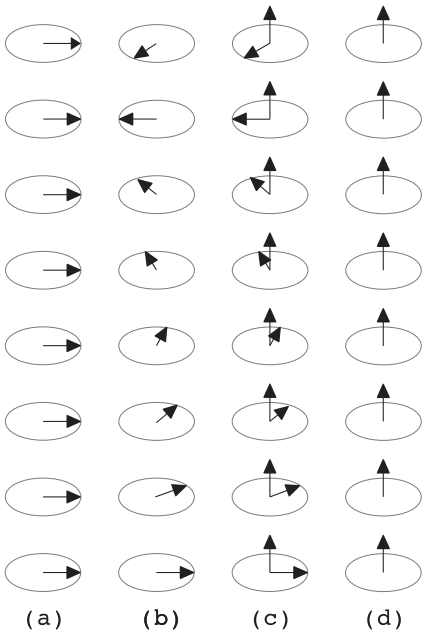

Fig. 2. Magnetic ordered structures of $\langle \boldsymbol{S}_n \rangle$: (a) ferromagnet ($\boldsymbol{Q} = \boldsymbol{0}$, $\theta = \pi/2$); (b) helix ($\boldsymbol{Q} \neq \boldsymbol{0}, \theta = \pi/2$); (c) cone ($\boldsymbol{Q} \neq \boldsymbol{0}, 0 < \theta < \pi/2$); (d) ferromagnet ($\boldsymbol{Q} \neq \boldsymbol{0}, \theta = 0$).

with a cone angle θ and a helical wave vector $\boldsymbol{Q}$ along the k_z axis as shown in Fig. 2 [3],

$$\langle \boldsymbol{S}_n \rangle = \langle S \rangle \, (\sin\theta \cos\phi_n, \sin\theta \sin\phi_n, \cos\theta). \tag{5}$$

where $\phi_n = (\boldsymbol{Q} \cdot \boldsymbol{R}_n)$ is the turn angle. This cone structure becomes the helical structure for $\theta = \pi/2$ and the ferromagnetic structure for $\theta = 0$ or $\boldsymbol{Q} = \boldsymbol{0}$.

If there is no crystalline anisotropy, the cone axis can be in any direction. For an anisotropy of easy plane the cone axis is the c-direction while for an anisotropy of easy c-axis, the situation is more complicated [5,20].

For the first transformation the local axes (ξ_n, η_n, ζ_n) are introduced at each site $\boldsymbol{R}_n$, where ζ_n is defined to be along the direction of the local moment $\langle \boldsymbol{S}_n \rangle$, ξ_n along the direction perpendicular to both ζ_n and z axes, and η_n along the direction perpendicular to ζ_n and η_n axes as shown in Fig. 3. Those unit vectors $\boldsymbol{e}_{n\xi}$, $\boldsymbol{e}_{n\eta}$, $\boldsymbol{e}_{n\zeta}$ are given by

$$\left.\begin{aligned} \boldsymbol{e}_{n\xi} &= (\cos\theta \cos\phi_n, \cos\theta \sin\phi_n, -\sin\theta), \\ \boldsymbol{e}_{n\eta} &= (-\sin\phi_n, \cos\phi_n, 0), \\ \boldsymbol{e}_{n\zeta} &= (\sin\theta \cos\phi_n, \sin\theta \sin\phi_n, \cos\theta). \end{aligned}\right\} \tag{6}$$

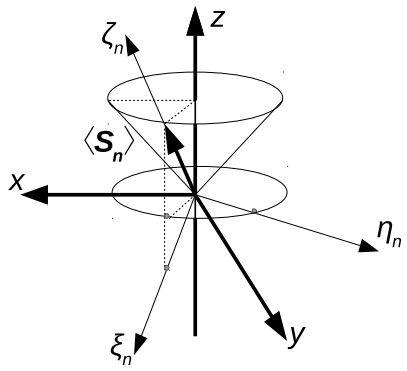

Fig. 3. Local coordinate axes (ξ_n, η_n, ζ_n).

Hence the f-spin operator $S_{n\xi}$, $S_{n\eta}$, $S_{n\zeta}$ are defined by

$$\boldsymbol{S}_n = S_{n\xi}\, \boldsymbol{e}_{n\xi} + S_{n\eta}\, \boldsymbol{e}_{n\eta} + S_{n\zeta}\, \boldsymbol{e}_{n\zeta}. \tag{7}$$

The unperturbed Hamiltonian H_0 is diagonalized by the transformation,

$$\left.\begin{aligned} A_{\boldsymbol{k}-} &= a_{\boldsymbol{k}\uparrow} \cos\theta_{\boldsymbol{k}} + a_{\boldsymbol{k}-\boldsymbol{Q}\downarrow} \sin\theta_{\boldsymbol{k}} \\ A_{\boldsymbol{k}+} &= -a_{\boldsymbol{k}\uparrow} \sin\theta_{\boldsymbol{k}} + a_{\boldsymbol{k}-\boldsymbol{Q}\downarrow} \cos\theta_{\boldsymbol{k}} \end{aligned}\right\} \tag{8}$$

with

$$\cos(2\theta_{\boldsymbol{k}}) = \frac{\varepsilon_{\boldsymbol{k}-\boldsymbol{Q}} - \varepsilon_{\boldsymbol{k}} + 2y}{\sqrt{(\varepsilon_{\boldsymbol{k}-\boldsymbol{Q}} - \varepsilon_{\boldsymbol{k}} + 2y)^2 + 4x^2}} \tag{9}$$

where $0 \leq \theta_{\boldsymbol{k}} \leq \frac{\pi}{2}$ and

$$x = I\langle S \rangle \sin\theta, \quad y = I\langle S \rangle \cos\theta\,. \tag{10}$$

After these two transformations, the Hamiltonian H_1 is rewritten as

$$\left.\begin{aligned} H &= H_0 + H_1 \\ H_0 &= \textstyle\sum_{\boldsymbol{k}\mu} E_{\boldsymbol{k}\mu} A^{\dagger}_{\boldsymbol{k}\mu} A_{\boldsymbol{k}\mu} \\ H_1 &= -IN^{-1} \textstyle\sum_{\boldsymbol{k}} \sum_{\boldsymbol{k}'} \sum_n \mathrm{e}^{\mathrm{i}(\boldsymbol{k}-\boldsymbol{k}')\cdot \boldsymbol{R}_n} \\ &\quad \times (A^{\dagger}_{\boldsymbol{k}-} \; A^{\dagger}_{\boldsymbol{k}+})(\sigma_-(\boldsymbol{k}, \boldsymbol{k}')S_{n+} \\ &\quad + \sigma_+(\boldsymbol{k}, \boldsymbol{k}')S_{n-} + \sigma_\zeta(\boldsymbol{k}, \boldsymbol{k}')S_{n0}) \\ &\quad \times \begin{pmatrix} A_{\boldsymbol{k}'-} \\ A_{\boldsymbol{k}'+} \end{pmatrix} \end{aligned}\right\} \tag{11}$$

where the new dispersion energy of the conduction electron $E_{\boldsymbol{k}\mu}$ is given by (see Fig. 10)

$$\begin{aligned} E_{\boldsymbol{k}\pm} = \frac{1}{2} [\, &\varepsilon_{\boldsymbol{k}} + \varepsilon_{\boldsymbol{k}-\boldsymbol{Q}} \\ &\pm \sqrt{(\varepsilon_{\boldsymbol{k}-\boldsymbol{Q}} - \varepsilon_{\boldsymbol{k}} + 2y)^2 + 4x^2}\,]. \end{aligned} \tag{12}$$

The f-spin operators $S_{n\pm}$ and S_{n0} are

$$S_{n\pm} = S_{n\xi} \pm \mathrm{i} S_{n\eta}, \quad S_{n0} = S_{n\zeta} - \langle S \rangle, \tag{13}$$

and the new spin matrices $\sigma_\pm(\boldsymbol{k}, \boldsymbol{k}')$ and $\sigma_\zeta(\boldsymbol{k}, \boldsymbol{k}')$ operating on the pseudo spin $\pm$ in $A_{\boldsymbol{k}\pm}$ are

$$\left.\begin{aligned} \sigma_-(\boldsymbol{k}, \boldsymbol{k}') &= \tfrac{1}{2}[\sigma_3 \sin(\theta_{\boldsymbol{k}} + \theta_{\boldsymbol{k}'} - \theta) \\ &\quad + \sigma_1 \cos(\theta_{\boldsymbol{k}} + \theta_{\boldsymbol{k}'} - \theta) \\ &\quad - \mathrm{i}\sigma_2 \cos(\theta_{\boldsymbol{k}} - \theta_{\boldsymbol{k}'}) \\ &\quad + 1 \sin(\theta_{\boldsymbol{k}} - \theta_{\boldsymbol{k}'})], \\ \sigma_+(\boldsymbol{k}, \boldsymbol{k}') &= \sigma_-(\boldsymbol{k}', \boldsymbol{k})^{\dagger}, \\ \sigma_\zeta(\boldsymbol{k}, \boldsymbol{k}') &= \sigma_3 \cos(\theta_{\boldsymbol{k}} + \theta_{\boldsymbol{k}'} - \theta) \\ &\quad - \sigma_1 \sin(\theta_{\boldsymbol{k}} + \theta_{\boldsymbol{k}'} - \theta), \end{aligned}\right\} \tag{14}$$

where σ_1, σ_2 and σ_3 are the usual Pauli spin matrices and 1 a unit matrix.

2.2 Magnetic phase diagram at $T = 0$

The unperturbed energy $\mathcal{E}_0$ at $T = 0$ is defined by a model of the fixed Fermi-energy in which the reservoir corresponds to other parts of Fermi surface,

$$\mathcal{E}_0 = \langle H_0 - E_f \widehat{N} \rangle = \int_{-\infty}^{E_f} \sum_{\boldsymbol{k},\mu} \frac{\gamma\ (\omega - E_f)}{(E_{\boldsymbol{k}\mu} - \omega)^2 + \gamma^2} \frac{\mathrm{d}\omega}{\pi}\ , \tag{15}$$

where $\widehat{N}$ is the number operator of the conduction electrons [20]. In the equilibrium state of the unperturbed system, the helical wavenumber Q_0 and the cone angle θ_0 are determined so as to minimize the energy

$$\mathcal{E}_0 = \mathcal{E}_0(\theta, Q : k_a, I\langle S\rangle, \gamma) \tag{16}$$

for a given set of the system parameters k_a, $I\langle S\rangle$ and γ. Hence the partial derivatives $\partial\mathcal{E}_0/\partial\theta$ and $\partial\mathcal{E}_0/\partial Q$ vanish at $Q = Q_0$ and $\theta = \theta_0$. The former is given by (Appendix C)

$$\frac{\partial \mathcal{E}_0}{\partial \theta} = -I\langle S\rangle \sum_{\boldsymbol{k}} (f_{\boldsymbol{k}-} - f_{\boldsymbol{k}+}) \sin(2\theta_{\boldsymbol{k}} - \theta) = 0, \tag{17}$$

where $f_{\boldsymbol{k}\pm} = f(E_{\boldsymbol{k}\pm})$ and $f(\varepsilon)$ is given by

$$f(\varepsilon) = \frac{1}{2} - \frac{1}{\pi} \tan^{-1} \frac{\varepsilon - E_f}{\gamma}. \tag{18}$$

Because the Fermi level should be in the gap created by the nesting, Q_0 and θ_0 satisfy the condition

$$|Q_0/Q_f - 1| \le I\langle S\rangle \sin\theta_0/E_f\ , \tag{19}$$

where the nesting wavenumber $Q_f = 2E_f/v_1$.

The non-dimensional quantities are introduced as

$$\left.\begin{aligned} &\widetilde{\mathcal{E}}_0 = (C/NE_f)\mathcal{E}_0, \quad C = 4\pi^3 v_1 {v_2}^2 N/{E_f}^3, \\ &\tilde{k}_a = k_a v_2/E_f, \quad \Delta = I\langle S\rangle/E_f, \quad \Gamma = \gamma/E_f, \\ &\widetilde{Q} = Q v_1/E_f, \quad \tilde{q}_z = q_z v_1/E_f, \quad \tilde{q}_x = q_x v_2/E_f. \end{aligned}\right\} \tag{20}$$

Then the above condition is rewritten as

$$|\widetilde{Q}_0/2 - 1| \le \Delta \sin\theta_0\ . \tag{21}$$

Figure 4 shows the magnetic phase diagrams at zero temperature for $\Gamma = 0$ and 0.01 [20]. For small c-f exchange interaction Δ, the helical structure ($\theta = \frac{\pi}{2}$, $\widetilde{Q}_0 \approx 2$) is realized because of flat Fermi surfaces perpendicular to the k_z-axis. When Δ increases in the region of $\tilde{k}_a < 1.2$, the cone structure ($0 < \theta < \frac{\pi}{2}$, $Q_0 > 0$) becomes more stable than the helix structure. The second-order helix-cone boundary is determined by

$$\partial^2\mathcal{E}_0/\partial\theta^2\big|_{\theta=\frac{\pi}{2},\widetilde{Q}=\widetilde{Q}_0} = 0\ , \tag{22}$$

and hence give by

$$\left.\begin{aligned} &\tfrac{7}{6} + \tilde{k}_a - \tilde{k}_a^2 \ln\tfrac{2}{\mathrm{e}\Delta} = 0, \text{ for } \Gamma \ll \Delta \ll 1\ , \\ &\tfrac{7}{6} + \tilde{k}_a - \tilde{k}_a^2 \ln\tfrac{1}{\mathrm{e}\Gamma} = 0, \text{ for } \Delta \ll \Gamma \ll 1\ . \end{aligned}\right\} \tag{23}$$

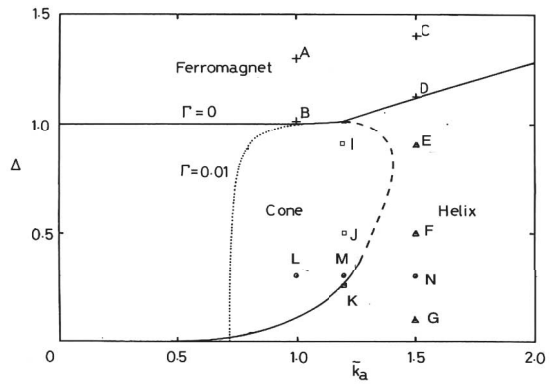

Fig. 4. Phase diagram for $\Gamma = 0$. The full curves represent the second-order transition boundaries and the broken curve the first-order transition boundary. The dotted curve is the second-order ferro-cone boundary for $\Gamma = 0.01$. Spin-wave dispersions are calculated at points A to N.

When Δ increases further and tends to unity in the region of $\tilde{k}_a < 1.2$, the cone structure becomes the ferromagnetic structure ($\theta = 0$). The second-order ferromagnet-cone transition boundary is determined by

$$\partial^2\mathcal{E}_0/\partial\theta^2\big|_{\theta=0,\widetilde{Q}=2} = 0\ . \tag{24}$$

For small value of Γ, this boundary is given by

$$\frac{1}{6}(7 - \Delta^2) + \tilde{k}_a - \tilde{k}_a^2 \ln\frac{\sqrt{1-\Delta^2}}{\mathrm{e}\Gamma} = 0\ , \tag{25}$$

and for $\Gamma = 0.01$ drawn by the dotted curve in Fig. 4. When Γ tends to zero, the ferro-cone boundary goes to $\Delta = 1$. The second-order ferro-cone transition boundary is sensitive to small value of the life time Γ, but the other boundaries change little.

When Δ increases in the region of $\tilde{k}_a > 1$, the helical wavenumber Q_0 tends to zero and the second-order helix-ferromagnet transition occurs. This transition boundary is detemined by

$$\partial^2\mathcal{E}_0/\partial Q^2\big|_{\theta=\frac{\pi}{2},\widetilde{Q}=0} = 0, \tag{26}$$

and hence given by

$$\frac{1}{3}(\Delta + 1)^2(2\Delta - 1) + (\Delta^2 - 1)\tilde{k}_a - \tilde{k}_a^2 = 0\ . \tag{27}$$

Setting $\Delta = 1$ in the above boundary, we obtain that $\tilde{k}_a$ is $\frac{2}{\sqrt{3}} \simeq 1.2$ at the tricritical point.

2.3 Effective f-spin Hamiltonian

In the second-order perturbation of H_1, the effective f-spin Hamiltonian H_S is obtained by

$$H_S = \langle H_1\rangle + \langle H_1(\mathcal{E}_0 - H_0)^{-1} H_1\rangle_{\mathrm{c}} \tag{28}$$

where the suffix c means the connected diagram. Applying the spin-wave method to H_S, we can derive magnon dispersions in the ferromagnet in Sec. 3, and the cone and the helix in Sec. 4.

3. Spin Wave in Ferromagnet

3.1 Effective f-spin Hamiltonian

The effective f-spin Hamiltonian in the ferromagnet is given by

$$\begin{aligned} H_S &= -J_0 \sum_n S_{n0} \\ &+N^{-1} \sum_n \sum_m \sum_{\boldsymbol{q}\neq\boldsymbol{0}} \mathrm{e}^{\mathrm{i}\,\boldsymbol{q}\cdot\boldsymbol{R}_{nm}} K(\boldsymbol{q}) S_{n0} S_{m0} \\ &-N^{-1} \sum_n \sum_m \sum_{\boldsymbol{q}} \mathrm{e}^{\mathrm{i}\,\boldsymbol{q}\cdot\boldsymbol{R}_{nm}} J_+(\boldsymbol{q}) \\ &\quad\times (S_{nx}S_{mx} + S_{ny}S_{my}) \\ &-N^{-1} \sum_{\boldsymbol{q}} J_-(\boldsymbol{q}) \sum_n S_{nz} \end{aligned} \tag{29}$$

where J_0, $K(\boldsymbol{q})$ and $J_\pm(\boldsymbol{q})$ are

$$\left.\begin{aligned} J_0 &= IN^{-1} \textstyle\sum_{\boldsymbol{k}} (f_{\boldsymbol{k}\uparrow} - f_{\boldsymbol{k}\downarrow}), \\ K(\boldsymbol{q}) &= I^2 N^{-1} \textstyle\sum_{\boldsymbol{k}} \sum_\sigma \dfrac{f_{\boldsymbol{k}\sigma}}{\varepsilon_{\boldsymbol{k}-\boldsymbol{q}\sigma} - \varepsilon_{\boldsymbol{k}\sigma}}, \\ J_\pm(\boldsymbol{q}) &= I^2 N^{-1} \textstyle\sum_{\boldsymbol{k}} \{ \dfrac{f_{\boldsymbol{k}\downarrow}(1-f_{\boldsymbol{k}-\boldsymbol{q}\uparrow})}{\varepsilon_{\boldsymbol{k}-\boldsymbol{q}\uparrow} - \varepsilon_{\boldsymbol{k}\downarrow}} \\ &\qquad \pm \dfrac{f_{\boldsymbol{k}\uparrow}(1-f_{\boldsymbol{k}-\boldsymbol{q}\downarrow})}{\varepsilon_{\boldsymbol{k}-\boldsymbol{q}\downarrow} - \varepsilon_{\boldsymbol{k}\uparrow}} \}, \end{aligned}\right\} \tag{30}$$

and σ means $\uparrow$ or $\downarrow$ in the σ sum and

$$\varepsilon_{\boldsymbol{k}\uparrow} = \varepsilon_{\boldsymbol{k}} - I\langle S\rangle, \quad \varepsilon_{\boldsymbol{k}\downarrow} = \varepsilon_{\boldsymbol{k}} + I\langle S\rangle. \tag{31}$$

From Eq. (18), $f_{\boldsymbol{k}\sigma} = f(\varepsilon_{\boldsymbol{k}\sigma})$ with the life time γ at $T = 0$. Note that

$$J_0 = 2\langle S\rangle J_+(\boldsymbol{0})\ . \tag{32}$$

3.2 Spin wave in ferromagnet at $T = 0$

At zero temperature, $\langle S\rangle$ is equal to S. The f-spin operators

$$S_{n\pm} = S_{nx} \pm \mathrm{i}S_{ny}, \quad S_{n0} = S_{nz} - S \tag{33}$$

are represented by the annihilation and creation magnon operators b_n and $b_n^\dagger$ [26]

$$\left.\begin{aligned} S_{n+} &= \sqrt{2S}\,(1 - b_n^\dagger b_n/2S)^{\frac{1}{2}} b_n, \\ S_{n-} &= \sqrt{2S}\, b_n^\dagger (1 - b_n^\dagger b_n/2S)^{\frac{1}{2}}, \\ S_{n0} &= -b_n^\dagger b_n. \end{aligned}\right\} \tag{34}$$

The Fourier transforms of the magnon operators are

$$\left.\begin{aligned} b_n &= N^{-\frac{1}{2}} \textstyle\sum_{\boldsymbol{q}} \mathrm{e}^{\mathrm{i}\,\boldsymbol{q}\cdot\boldsymbol{R}_n} b_{\boldsymbol{q}}, \\ b_n^\dagger &= N^{-\frac{1}{2}} \textstyle\sum_{\boldsymbol{q}} \mathrm{e}^{-\mathrm{i}\,\boldsymbol{q}\cdot\boldsymbol{R}_n} b_{\boldsymbol{q}}^\dagger\ . \end{aligned}\right\} \tag{35}$$

After expanding the square-roots of Eq. (34) with $1/S$ and taking only terms of the first order of S, the Hamiltonian H_S is rewritten as

$$H_S = E_0 + \sum_{\boldsymbol{q}} \omega_0(\boldsymbol{q})\, b_{\boldsymbol{q}}^\dagger\, b_{\boldsymbol{q}}, \tag{36}$$

and the spin wave dispersion is given by

$$\omega_0(\boldsymbol{q}) = 2S\,[J_+(\boldsymbol{0}) - J_+(\boldsymbol{q})]\ , \tag{37}$$

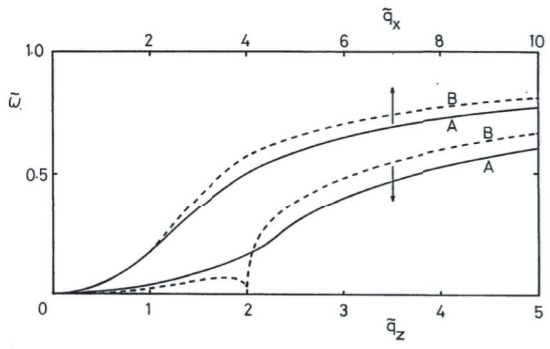

Fig. 5. Ferromagnetic magnon dispersions along q_z and q_x axes for $\tilde{k}_a = 1.0$ and $\Gamma = 0$: Full curves A correspond to $\Delta = 1.3$, broken curves B to $\Delta = 1.01$. $\tilde{\omega} = \omega_0/J_0$.

and E_0 is a constant $-S\sum_{\boldsymbol{q}}[J_+(\boldsymbol{q}) + J_-(\boldsymbol{q})]$.

For the ferromagnetic structure to be stable, all the frequencies must be positive. In particular the frequency near $\boldsymbol{q} = \boldsymbol{0}$ tends to zero on the second-order ferromagnet-helix boundary, and the frequency at $\boldsymbol{q} = \boldsymbol{Q}_f = (0, 0, Q_f)$ tends to zero on the second-order ferromagnet-cone boudary.

The frequency $\omega_0(\boldsymbol{q})$ is quadratic in $\boldsymbol{q} = (q_x, q_y, q_z)$ for small $\boldsymbol{q}$

$$\omega_0(q_x, 0, q_z) \simeq D_1 q_z{}^2 + D_2 q_x{}^2. \tag{38}$$

The spin wave constant D_1 is obtained by the formula (Appendix A),

$$D_1 = \frac{1}{4NS} \sum_{\boldsymbol{k}\sigma} f_{\boldsymbol{k}\sigma} \left[\frac{\partial^2 \varepsilon_{\boldsymbol{k}}}{\partial k_z{}^2} - \frac{\sigma}{IS} \left(\frac{\partial \varepsilon_{\boldsymbol{k}}}{\partial k_z} \right)^2 \right]. \tag{39}$$

By use of the band model of Eq. (3), this formula is rewritten as the simpler formula of Eq. (A.4).

3.3 Spin-wave dispersion near the ferromagnet-cone boundary

Near the ferromagnet-cone boundary, the spin-wave dispersion shows a sharp dip around $\boldsymbol{q} = \boldsymbol{Q}_f$. A small lifetime weakens the logarithmic divergence of the frequency at $q = Q_f$ near $\Delta = 1$ and thus makes the ferromagnet stable even for $\Delta < 1$.

The spin-wave frequency at $\boldsymbol{Q}_0 = (0, 0, Q_0)$ is given by (Appendix C (7))

$$\omega_0(\boldsymbol{Q}_0) = \frac{1}{NS} \lim_{\theta_0 \to 0} \frac{\partial^2 \mathcal{E}_0(\theta_0, \boldsymbol{Q}_0)}{\partial \theta^2}\ . \tag{40}$$

When Γ tends to zero, Q_0 goess to Q_f and hence $\omega_0(\boldsymbol{Q}_0)$ vanishes on the ferro-cone boundary from Eq. (24). Spin-wave dispersions along the q_z and q_x axes are shown in Fig. 5.

For the ferromagnet for $\Delta < 1$ with a small value of Γ, the magnon dispersion has the quadratic form

$$\omega_0(q_x, 0, q_z) \approx D_1\, q_z{}^2 + D_2\, q_x{}^2, \tag{41}$$

for $\tilde{q}_z < 1 - \Delta$ and for $\tilde{q}_x < \min\{1 - \Delta, 2\tilde{k}_a\}$. The spin-wave constants are given by

$$D_1 = \left(\frac{v_1}{v_2} \right)^2 D_2, \quad D_2 = \frac{I^2 S}{6\pi^3 v_1 N}, \tag{42}$$

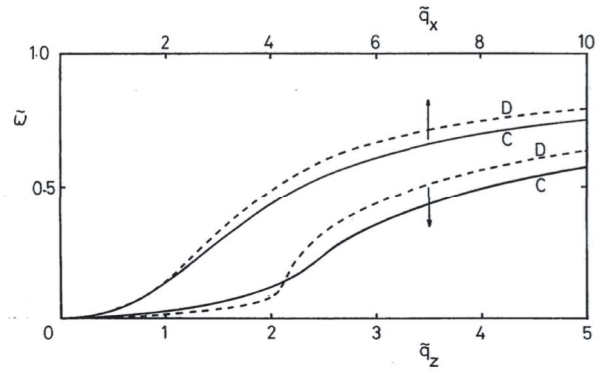

Fig. 6. Ferromagnetic magnon dispersions along q_z and q_x axes for $\tilde{k}_a = 1.5$ and $\Gamma = 0$: Full curves C correspond to $\Delta = 1.4$, broken curves D to $\Delta = 1.12$. $\tilde{\omega} = \omega_0/J_0$.

and independent of $\tilde{k}_a$. Note that a small value of Γ has very small effect on the spin-wave constants.

3.4 Spin wave near the ferromagnet-helix transition boundary

For $\Delta > 1$, the perfect splitting of up- and down-spin bands is realized and hence the up-spin band becomes empty. Using Eq. (A.4), we obtain the spin wave constants given by

$$D_1 = \frac{I}{2C\Delta^2}\left(\frac{v_1}{E_f}\right)^2 \times \left[\frac{1}{3}(2\Delta-1)(\Delta+1)^2 + (\Delta^2-1)\tilde{k}_a - \tilde{k}_a^2\right], \tag{43}$$

$$D_2 = \frac{I}{2C\Delta^2}\left(\frac{v_2}{E_f}\right)^2 \times \left[\frac{1}{3}(2\Delta^3-1) + (\Delta^2-1)\tilde{k}_a\right]. \tag{44}$$

When $\tilde{k}_a$ increases for $\Delta > 1$, D_1 decreases and tends to zero on the ferromagnet-helix boundary of Eq. (27). The softening of D_1 means the formation of helical component with an infinitesimal value of Q_0 on this boundary. Figure 6 shows the dispersion curves at C and D in Fig. 4. When the ferromagnetic state tends to the ferro-helix boundary, its dispersion along the q_z becomes flat in the region of $0 < \tilde{q}_z < \tilde{Q}_f = 2$, while it increases rapidly in the region of $\tilde{q}_z > 2$, and hence a sharp kink appears at $\tilde{q}_z = 2$.

The dispersions near the ferro-cone-helix tricritical point are shown in 4.5.

4. Spin Waves in Conical and Helical Structures

4.1 Effective f-spin Hamiltonian

From Eq. (28) the effective f-spin Hamiltonian H_S consists of the first-order and the second-order contributions. By use of Eq. (17) the first-order contribution is given by

$$-\mathcal{J}_0 \sum_n S_{n0} \tag{45}$$

where $S_{n0} = S_{n\zeta} - \langle S\rangle$ and

$$\mathcal{J}_0 = \frac{I}{N}\sum_{\boldsymbol{k}} (f_{\boldsymbol{k}-} - f_{\boldsymbol{k}+})\cos(2\theta_{\boldsymbol{k}} - \theta) \tag{46}$$

with $f_{\boldsymbol{k}\pm} = f(E_{\boldsymbol{k}\pm})$. The second-order contribution is represented by

$$-\frac{1}{N}\sum_n\sum_m\sum_{\boldsymbol{q}} e^{i\,\boldsymbol{q}\cdot\boldsymbol{R}_{nm}}(S_{n\xi}, S_{n\eta}, S_{n0}) \times \begin{pmatrix} \mathcal{J}_{11}(\boldsymbol{q}) & i\mathcal{J}_{12}(\boldsymbol{q}) & \mathcal{J}_{13}(\boldsymbol{q}) \\ -i\mathcal{J}_{12}(\boldsymbol{q}) & \mathcal{J}_{22}(\boldsymbol{q}) & i\mathcal{J}_{23}(\boldsymbol{q}) \\ \mathcal{J}_{13}(\boldsymbol{q}) & -i\mathcal{J}_{23}(\boldsymbol{q}) & \mathcal{J}_{33}(\boldsymbol{q}) \end{pmatrix} \begin{pmatrix} S_{m\xi} \\ S_{m\eta} \\ S_{m0} \end{pmatrix}. \tag{47}$$

The f-f exchange matrix elements $\mathcal{J}_{ij}(\boldsymbol{q})$ are given in Appendix B. Note that $\mathcal{J}_{ij}(\boldsymbol{q})$'s are not continuous at $\boldsymbol{q} = \boldsymbol{0}$ except for $\mathcal{J}_{22}(\boldsymbol{q})$.

4.2 Spin waves in cone and helix at $T = 0$

The cone structure of Eq. (5) becomes the helix when $\theta = \frac{\pi}{2}$ and the ferromagnet when $\theta = 0$ or $Q = 0$ (see Fig. 2). Neglecting the quantum correction to $S_{n\zeta}$ at zero temperature, we put $\langle S\rangle = S$.

When (S_{nx}, S_{ny}, S_{nz}) are replaced by $(S_{n\xi}, S_{n\eta}, S_{n\zeta})$ in Eqs. (33) and (34), the magnon energy is calculated in the same way as the case of the ferromagnet. Expanding H_S with $1/S$ and retaining the terms up to the order of S, we obtain

$$H_S = E_0 + \sum_{\boldsymbol{q}} [2A_{\boldsymbol{q}}\, b^\dagger_{\boldsymbol{q}}\, b_{\boldsymbol{q}} + B_{\boldsymbol{q}}\,(b^\dagger_{\boldsymbol{q}}\, b^\dagger_{-\boldsymbol{q}} + b_{\boldsymbol{q}}\, b_{-\boldsymbol{q}})] \tag{48}$$

where E_0 is a constant and $A_{\boldsymbol{k}}$ and $B_{\boldsymbol{k}}$ are

$$\left.\begin{aligned} 2A_{\boldsymbol{q}} &= \mathcal{J}_0 - S[\mathcal{J}^+_{11}(\boldsymbol{q}) + \mathcal{J}^+_{22}(\boldsymbol{q})] \\ &\quad -2S\mathcal{J}^-_{12}(\boldsymbol{q}), \\ 2B_{\boldsymbol{q}} &= -S[\mathcal{J}^+_{11}(\boldsymbol{q}) - \mathcal{J}^+_{22}(\boldsymbol{q})] \end{aligned}\right\} \tag{49}$$

and $\mathcal{J}^\pm_{ij}$ are

$$\mathcal{J}^\pm_{ij}(\boldsymbol{q}) = \frac{1}{2}[\mathcal{J}_{ij}(\boldsymbol{q}) \pm \mathcal{J}_{ij}(-\boldsymbol{q})]. \tag{50}$$

By the well-known transformation [4]

$$\left.\begin{aligned} \beta_{\boldsymbol{q}} &= b_{\boldsymbol{q}}\cosh\phi_{\boldsymbol{q}} + b^\dagger_{-\boldsymbol{q}}\sinh\phi_{\boldsymbol{q}} \\ \beta^\dagger_{\boldsymbol{q}} &= b^\dagger_{\boldsymbol{q}}\cosh\phi_{\boldsymbol{q}} + b_{-\boldsymbol{q}}\sinh\phi_{\boldsymbol{q}} \end{aligned}\right\} \tag{51}$$

with the conditions $\phi_{-\boldsymbol{q}} = \phi_{\boldsymbol{q}}$ and

$$(A_{\boldsymbol{q}} + A_{-\boldsymbol{q}})\sinh 2\phi_{\boldsymbol{q}} = 2B_{\boldsymbol{q}}\cosh 2\phi_{\boldsymbol{q}}, \tag{52}$$

H_S is diagonalized as

$$H_S = E_1 + \sum_{\boldsymbol{q}} \omega(\boldsymbol{q})\beta^\dagger_{\boldsymbol{q}}\,\beta_{\boldsymbol{q}}, \tag{53}$$

where E_1 is a constant. The magon energy $\omega(\boldsymbol{q})$ is given by

$$\omega(\boldsymbol{q}) = C(\boldsymbol{q}) + \sqrt{F_1(\boldsymbol{q})\cdot F_2(\boldsymbol{q})} \tag{54}$$

where $F_1(\boldsymbol{q})$, $F_2(\boldsymbol{q})$ and $C(\boldsymbol{q})$ are

$$\left.\begin{aligned} F_1(\boldsymbol{q}) &= A_{\boldsymbol{q}} + A_{-\boldsymbol{q}} + 2B_{\boldsymbol{q}} \\ &= \mathcal{J}_0 - 2S\mathcal{J}^+_{11}(\boldsymbol{q}), \\ F_2(\boldsymbol{q}) &= A_{\boldsymbol{q}} + A_{-\boldsymbol{q}} - 2B_{\boldsymbol{q}} \\ &= \mathcal{J}_0 - 2S\mathcal{J}^+_{22}(\boldsymbol{q}), \\ C(\boldsymbol{q}) &= A_{\boldsymbol{q}} - A_{-\boldsymbol{q}} = -2S\mathcal{J}^-_{12}(\boldsymbol{q}). \end{aligned}\right\} \tag{55}$$

Note that $F_1(\boldsymbol{q})$ and $F_1(\boldsymbol{q})$ are even functions of $\boldsymbol{q}$ but $C(\boldsymbol{q})$ an odd function. The Fourier transforms of f-spin operators $S_{\boldsymbol{q}\xi}$ and $S_{\boldsymbol{q}\eta}$ are given by (Appendix C (1))

$$\left.\begin{aligned} S_{\boldsymbol{q}\xi} &\simeq \sqrt{\tfrac{S}{2}}\left[\frac{F_2(\boldsymbol{q})}{F_1(\boldsymbol{q})}\right]^{1/4}(\beta_{\boldsymbol{q}} + \beta^{\dagger}_{-\boldsymbol{q}}), \\ \mathrm{i}S_{\boldsymbol{q}\eta} &\simeq \sqrt{\tfrac{S}{2}}\left[\frac{F_1(\boldsymbol{q})}{F_2(\boldsymbol{q})}\right]^{1/4}(\beta_{\boldsymbol{q}} - \beta^{\dagger}_{-\boldsymbol{q}}). \end{aligned}\right\} \tag{56}$$

4.3 Modes of oscillations

One of special cases of interest is the situation near $\boldsymbol{q} = \boldsymbol{0}$. Using analogies from the Heisenberg model, we can obtain the following relations (Appendix C (2) and (3))

$$\lim_{\boldsymbol{q}\to\boldsymbol{0}} F_1(\boldsymbol{q}) = F_1(\boldsymbol{0}^+) = \frac{1}{NS}\frac{\partial^2}{\partial\theta^2}\mathcal{E}_0(\theta_0, \boldsymbol{Q}_0), \tag{57}$$

$$\lim_{\boldsymbol{q}\to\boldsymbol{0}} F_2(\boldsymbol{q}) = F_2(\boldsymbol{0}) = \frac{\cot\theta}{NS}\frac{\partial}{\partial\theta}\mathcal{E}_0(\theta_0, \boldsymbol{Q}_0). \tag{58}$$

For the stable cone structure, the first derivative of $\mathcal{E}_0$ with respect to θ should vanish. Hence $F_2(\boldsymbol{q})$ and $C(\boldsymbol{q})$ should vanish as $\boldsymbol{q} \to \boldsymbol{0}$ so that $\omega(\boldsymbol{q})$ becomes zero as $\boldsymbol{q} \to \boldsymbol{0}$ and so $S_{\boldsymbol{q}\xi}$ from Eq. (56). The mode of this oscillation is such that the whole spin system rotates as a rigid body around the helical axis.

Another special case of interest is the case of $\boldsymbol{q} = \pm\boldsymbol{Q}_0$, in which we can obtain the relation (Appendix C (4))

$$F_1(\boldsymbol{Q}_0) = F_2(\boldsymbol{Q}_0)\cos^2\theta_0\ . \tag{59}$$

In the helical phase ($\theta = \frac{\pi}{2}$), $C(\boldsymbol{q})$ and $F_1(\boldsymbol{q})$ vanish at $\boldsymbol{q} = \pm\boldsymbol{Q}_0$ and so $\omega(\boldsymbol{q})$, where $S_{\boldsymbol{q}\eta}$ also vanishes and $S_{\boldsymbol{q}\xi}$ diverges from Eq. (56). The mode of this oscillation is a small canting of the plane in which the spin vector rotates. In the cone phase, $C(\boldsymbol{q})$ makes a complicated dispersion but there is some similarity to the ferromagnetic case as shown in 4.5 and 4.6. From Eqs. (7) and (56), the lowering operator $S^- = \sum_n (S_{nx} - \mathrm{i}S_{ny})$ is represented by (Appendix C (5))

$$S^- \simeq NS\sin\theta_0\,\delta_{\boldsymbol{Q}_0,\boldsymbol{0}} + \sqrt{2NS\cos\theta_0}\,\beta^{\dagger}_{-\boldsymbol{Q}_0}. \tag{60}$$

Firstly the mode of oscillation for $\boldsymbol{q} = -\boldsymbol{Q}_0$ is such that the cone rotates as a rigid body about a certain axis in the xy-plane and hence no energy change should be associated with this motion (Appendix C (6)) as can be seen from Eq. (60) [27]. Secondly, for $\boldsymbol{q} = +\boldsymbol{Q}_0$, the motion of the cone includes a bending oscillation of the conical surface and hence the frequency is not necessarily zero (Appedix C (6)). Finally on the ferro-cone boundary, the conical magnon coincides with the ferromagnetic magnon of the wavevector shifted by $\boldsymbol{Q}_0$ as seen from Eq. (60).

For the assumed conical structure to be stable, the frequency must be positive for all values of $\boldsymbol{q}$, implying that the product $F_1(\boldsymbol{q}) \cdot F_2(\boldsymbol{q})$ should be positive. In the following subsections, we calculate numerically the dispersion $\omega(\boldsymbol{q})$ and two velocities in the cone phase, v_+ and v_- for $q_z > 0$ and $q_z < 0$ respectively. The velocities $v_\pm$ which are given by

$$v_\pm = \lim_{q_z\to\pm 0}\frac{\partial\omega}{\partial q_z} = v \pm u. \tag{61}$$

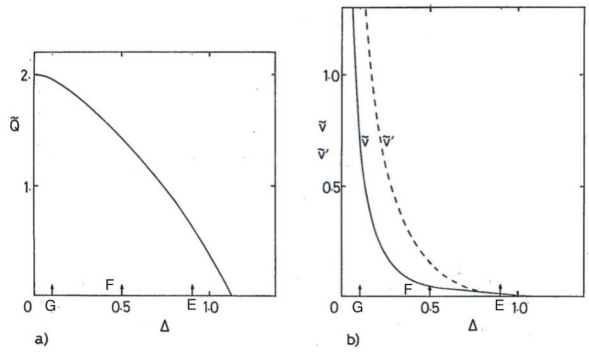

Fig. 7. Δ dependences of the wavenumber $\widetilde{Q}$ and the magnon velocities v and v' along the line $\tilde{k}_a = 1.5$ in Fig. 4.

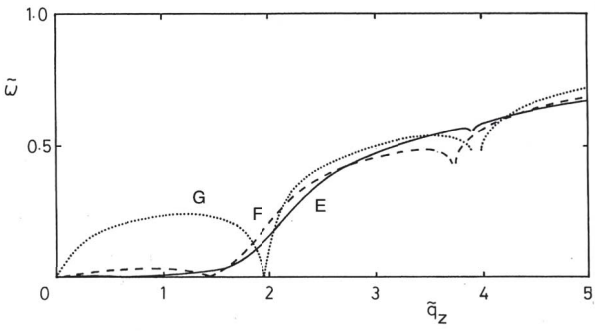

Fig. 8. Helical magnon dispersions for $\tilde{k}_a = 1.5$ and $\Gamma = 0$: Full curve E corresponds to $\Delta = 0.9$, broken curve F to $\Delta = 0.5$, dotted curve G to $\Delta = 0.1$. See triangles in Fig. 4 and arrows in Fig. 7.

show interesting behavior due to the non-linear c-f exchange effect, particularly near the phase boundaries. Note that in the Heisenberg model u always vanishes because $C(\boldsymbol{q})$ is given by

$$C(\boldsymbol{q}) = \frac{1}{2}\left[J(\boldsymbol{Q}_0 - \boldsymbol{q}) - J(\boldsymbol{Q}_0 + \boldsymbol{q})\right]\cos\theta \tag{62}$$

and $J(\boldsymbol{q})$ has a maximum at $\boldsymbol{q} = \boldsymbol{Q}_0$ [4].

In the following subsections, we show magnon dispersions of conical and helical states. For convenience, we use the reduced quantities,

$$\tilde{\omega} = \frac{\omega}{J_0}, \quad (\tilde{v}_\pm, \tilde{v}, \tilde{u}) = (v_\pm, v, u)\frac{E_f}{v_1 J_0}, \tag{63}$$

and denote θ_0 and Q_0 by θ and Q.

4.4 Dispersions near helix-ferromagnet boundary

When Δ increases along the line of $\tilde{k}_a = 1.5$, the helical structure changes to the ferromagnet. With increasing of Δ, $\widetilde{Q}$ decreases gradually, while two z-component velocities v at $q_z = 0$ and v' at $q_z = Q$ decrease rapidly and tends to zero on the helix-ferro boundary as shown in Fig. 7. Figure 8 shows that near the boundary, all the frequencies for $0 < q_z < Q_0$ show softening and a kink appears at $q_z = Q_f$. Finally, the whole shape of the dispersion changes smoothly to the ferromagnetic dispersion (see curve D in Fig. 6.)

4.5 Dispersions on helix-cone-ferromagnet transition line

With increasing of Δ along the line $\tilde{k}_a = 1.2$, the spin configuration changes from the helix to the cone, and,

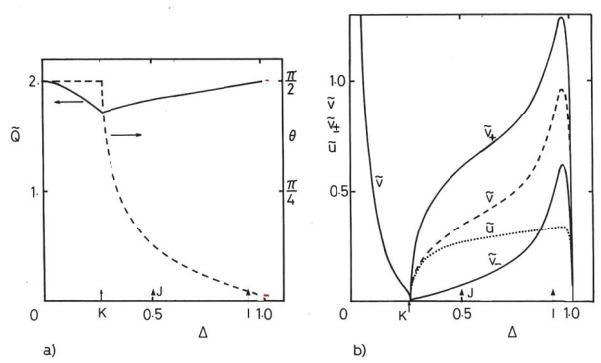

Fig. 9. Δ dependences of the wavenumber $\widetilde{Q}$, the cone angle θ and velocities $v_{\pm}$, v and u along the line $\tilde{k}_a = 1.2$ in Fig. 4.

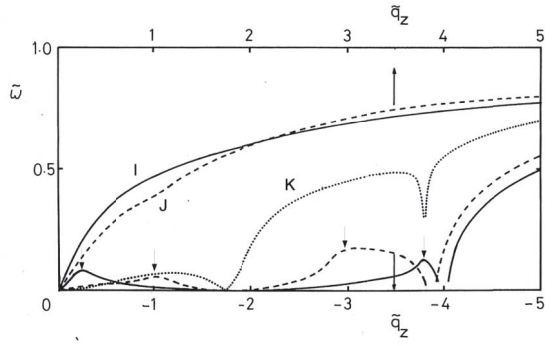

Fig. 10. Magnon dispersions in the cone, helix and the ferromagnetic phases for $\tilde{k}_a = 1.2$ and $\Gamma = 0$: Full curves I correspond to $\Delta = 0.9$, broken curves J to $\Delta = 0.6$, dotted curves K to $\Delta = 0.26$. Short arrows are peaks on curves I and J. See squares in Fig. 4 and arrows in Fig. 9.

through a narrow region of the helix again near the tricritical point, changes finally into the ferromagnet (see Fig. 4). Figure 9(a) shows that the second-order helix-ferro transition occurs on the condition that $\widetilde{Q}$ tends to zero, and the cone-helix transition around $\Delta = 1.0$ is of the first-order from ($\theta \sim 0, \widetilde{Q} \sim 2$) to ($\theta \sim \pi/2, \widetilde{Q} \sim 0$). Note that the cone-ferro boundary is nearly of the second-order as θ goes to zero. Figure 9(b) shows the values of θ, $\widetilde{Q}$ and the z-component velocities at $q = 0$ as functions of Δ. The velocities $v_{\pm}$ becomes zero on the second-oder helix-cone boundary. When Δ increases, $v_{\pm}$ increase rapidly and finally vanish on the ferromagnetic boundary again. The behavior of $v_{\pm}$ near the cone-helix-ferro tricritical point is similar to the second-order cone-ferro transition. Even though both θ and Q change drastically in both the states divided by the first-order cone-helix transition, both the states are similar and nearly continuous in the sense that both are continuously approaching to the common ferromagnetic ordering. The magnon dispersion is also nearly continuous at this first-order transition. Three examples of the magnon dispersions are shown in Fig. 10.

Figure 10 shows that each of magnon dispersions denoted by I and J has two peaks around $(-Q_+)$ and $(-Q_-)$. Both $Q_{\pm}$ connect the bottom of the upper band to the Fermi level of the lower band as shown in Fig. 11 and hence are given

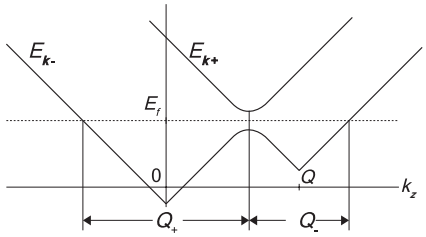

Fig. 11. The upper band E_{k+} and the lower band E_{k-}, and $Q_{\pm}$ that connects the bottom of E_{k+} and the Fermi level of E_{k-}.

by

$$\widetilde{Q}_{\pm} = \frac{v_1 Q_{\pm}}{E_f} = \frac{1}{2}\widetilde{Q} \pm \tilde{y} + \sqrt{\left(\frac{1}{2}\widetilde{Q} \pm \tilde{y}\right)^2 + \tilde{x}^2}, \quad (64)$$

where $\tilde{x} = \Delta \sin\theta$ and $\tilde{y} = \Delta \cos\theta$. When Δ increases in the cone phase, the region of quadratic dispersion between these two peaks extends and the spin-wave constant at $q_z = -Q$ decreases. At the same time, the region of the linear dispersion around $q_z = 0$ shrinks. The whole shape of the conical dispersion approaches to the ferromagnetic dispersion (see curve D in Fig. 6). Note that translating the magnon dispersion of the cone by $Q = Q_f$ to the q_z direction is needed to obtain the magnon dispersion of the ferromagnet on the cone-ferro boundary.

4.6 Dispersions near the cone-helix boundary

With decreasing of $\tilde{k}_a$ along the line $\Delta = 0.3$, the spin configuration changes from the helix to the cone, and finally to the ferromagnet for small value of Γ. Figure 12 shows the cone angle θ, the helical wavenumber $\widetilde{Q}$ and the z-component velocities at $q = 0$. The velocities tends to zero on the cone-helix boundary and diverge on the ferro-cone boundary, which exists in a finite $\tilde{k}_a$ for a small Γ (see Fig. 4). Figure 13 shows three magnon dispersions along the q_z direction for $\Delta = 0.3$. For the cone state, the dispersion L shows two peaks marked by arrows at $-Q_{\pm}$ given by Eq. (64). In the helix or the cone phase, the magnon energies show softening at $q_z = \pm(Q_+ + Q_-)$ (see Fig. 11) and hence for a small value of Γ they becomes unstable. This means that the higher harmonics are produced as discussed in Ref. [20]. This is, however, very sensitive to fine structures of the flat Fermi surfaces and thus we do not treat this problem here.

5. Spin Wave at Finite Temperature

We attempt to extend the formulae of spin waves at $T = 0$ to finite temperature. First of all, the spin configuration is determined by minimizing the unperturbed free energy $\mathcal{F}_0$ instead of $\mathcal{E}_0$, which may be written in the molecular field approximation as

$$\mathcal{F}_0 = -T \sum_{\boldsymbol{k}\mu} \times \ln\left(1 + \exp\{-[E_{\boldsymbol{k}\mu}(\langle S_\zeta\rangle, \theta, Q) - E_f]/T\}\right) - T\mathcal{S}(\langle S_\zeta\rangle) \quad (65)$$

where $\langle S_\zeta\rangle$, θ and Q are the variational parameters and the second term is the entropy of the f-spin system. The

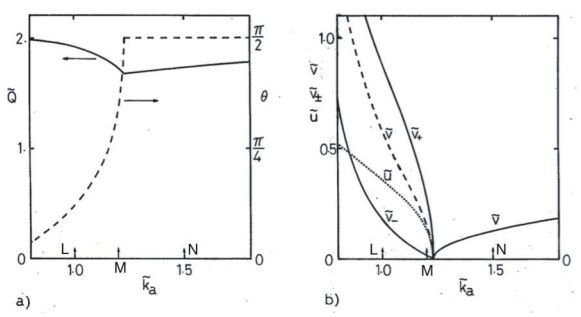

Fig. 12. $\tilde{k}_a$ dependences of the cone angle θ, the wavenumber $\tilde{Q}$ and velocities $\tilde{v}_\pm$, $\tilde{v}$ and $\tilde{u}$ for $\Delta = 0.3$.

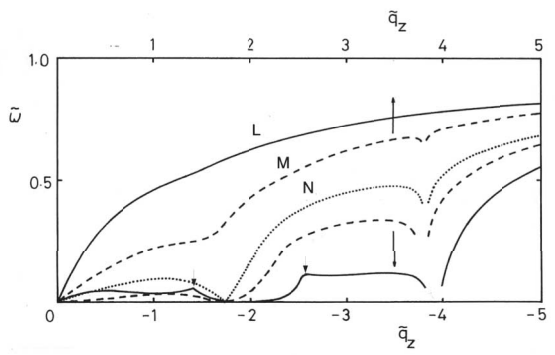

Fig. 13. Magnon dispersions for the cone and the helix for $\Delta = 0.3$. Full curves L correspond to $\tilde{k}_a = 1.0$, broken curves M to $\tilde{k}_a = 1.2$, dotted curve N to $\tilde{k}_a = 1.5$. Short arrows are two peaks on curve L. See circles in Fig. 4 and arrows in Fig. 12.

magnon dispersion is given by the same equations such as Eq. (37) by replacing S by $\langle S_\zeta \rangle$ if we assume that $\langle S_\zeta \rangle$ does not depend on θ and Q and the entropy of the conduction electrons is negligible compared with that of f-spins. This approximation seems to be not so bad because the ordered temperature is not so high and the ordered energy does not seem to depend so much on θ and Q. The same result is obtained by the following treatment.

Let us consider the case of the ferromagnet, for example, and introduce the double-time Green function given by [28]

$$G_{nm}(t) = \langle\langle S_{n+}(t); S_{m-}\rangle\rangle \tag{66}$$

where the up- and down-spin operators $S_{n\pm}$ are given by Eq. (33). Then the equation of motion of this Green function is

$$\begin{aligned} \mathrm{i}\frac{\partial}{\partial t} G_{nm}(t) &= 2\langle S\rangle\, \delta_{nm}\, \delta(t) + J_0\, G_{nm}(t) \\ &+ N^{-1} \sum_l \sum_{\boldsymbol{q}\neq \boldsymbol{0}} \exp(\mathrm{i}\, \boldsymbol{q}\cdot\, \boldsymbol{R}_{nl}) \\ &\times K(\,\boldsymbol{q})\langle\langle S_{n+}(t) S_{l0}(t) + S_{l0}(t) S_{n+}(t); S_{m-}\rangle\rangle \\ &- N^{-1} \sum_l \sum_{\boldsymbol{q}} \exp(\mathrm{i}\, \boldsymbol{q}\cdot\, \boldsymbol{R}_{nl}) \\ &\times [J_+(\,\boldsymbol{q})\langle\langle S_{nz}(t) S_{l+}(t) + S_{l+}(t) S_{nz}(t); S_{m-}\rangle\rangle \\ &- J_-(\,\boldsymbol{q})\langle\langle S_{nz}(t) S_{l+}(t) - S_{l+}(t) S_{nz}(t); S_{m-}\rangle\rangle]. \end{aligned} \tag{67}$$

The higher-order Green functions may be decoupled as [29]

$$\langle\langle S_{n+}(t) S_{lz}(t); S_{m-}\rangle\rangle \simeq \langle S_z\rangle \langle\langle S_{n+}(t); S_{m-}\rangle\rangle. \tag{68}$$

From the Fourier transform of the Green function

$$\begin{aligned} G(\,\boldsymbol{q}, E) &= \frac{1}{N}\sum_n \int G_{nm}(t) \mathrm{e}^{\mathrm{i}(Et - \boldsymbol{q}\cdot \boldsymbol{R}_{nm})} \frac{\mathrm{d}t}{2\pi} \\ &= \frac{1}{\pi} \frac{\langle S_z\rangle}{E - \omega_0(\,\boldsymbol{q})}, \end{aligned} \tag{69}$$

the excitation energy is obtained as

$$\omega_0(\,\boldsymbol{q}) = 2\langle S_z\rangle [J_+(\boldsymbol{0}) - J_+(\,\boldsymbol{q})]\,. \tag{70}$$

Following Tahir-Kheli and ter Haar [30] we can calculate the magnetization as a function of

$$\Phi(\langle S_z\rangle) = \frac{1}{N}\sum_{\boldsymbol{q}} \frac{1}{\exp(\omega_0(\,\boldsymbol{q})/T) - 1}. \tag{71}$$

Defining the Curie temperature T_C at which the magnetization $\langle S\rangle$ tends to zero, we obtain

$$T_C{}^{-1} = \frac{3}{2}\frac{1}{S(S+1)}\frac{1}{N}\sum_{\boldsymbol{q}} \frac{1}{J_+(\boldsymbol{0}) - J_+(\,\boldsymbol{q})}\,. \tag{72}$$

For other phases to which the same treatment is applicable, the spin-wave formula at finite temperature is obtained from Eq. (54) at $T = 0$ by replacing S and $\mathcal{E}_0$ by $\langle S\rangle$ and $\mathcal{F}_0$, respectively. The temperature effect is included in $\langle S\rangle$ and γ. Properties of spin-wave dispersions in finite temperature are discussed in Sec. 6.

6. Discussion and Conclusions

The present model is too simple to compare calculated spin-wave dispersions with experimental results in rare-earth metals, but semi-quantitive comparison is possible as shown in Ref. [20]. To remove any ambiguity, we have to neglect an additional Heisenberg-type exchange term which comes from another part of the Fermi surfaces and bands. As mentioned in Sec. 1, E_f and I are assumed to be 0.24 eV and 0.097 eV, respectively.

Based on the facts that v_2 should be chosen to be smaller than v_1 in order to fit the electronic specific heat and that k_a is larger than Q_f from the band calculation, $\tilde{k}_a$ is expected to be larger than unity and hence chosen to be 1.8 (see Fig. 1). The value of Γ at $T = 0$ K, Γ_0, is chosen tentatively to be 0.2 for Gd, which is mostly due to ripples of the Fermi surfaces. The temperature dependence of Γ is more important in the following discussions.

Table 1 shows a list of important parameters for each of rare-earth metals [20]. Here, for the crystal field, only the lowest-oder term V_2^0 is shown. Figure 14 shows phase diagrams for $\Gamma = 0.1$ to 0.4 [20]. When Γ increases, the second-order ferro-cone boundary moves rapidly to the larger value of $\tilde{k}_a$ and the cone region disappears while the ferro-helix bounday becomes the first-order.

First we consider Gd because the crystal field anisotropy is negligible. In Table 1, $\tilde{k}_a$ is assumed to be 1.8 and Δ_0 to be 1.4. Hence the value of Δ is 1.4 or 1.0 and the value of Γ is 0.2 or 0.3 for $T/T_C = 0$ or 0.7, respectively. As shown in Fig. 14, the ferromagnetic state of Gd moves downward along the vertical line from a cross 'a' as the temperature increases from $T = 0$ K.

Table 1. Spin values S, reduced crystal-field energy $\widetilde{V} = V_2^0 J^2/E_f$, reduced c-f exchange energy Δ_0 at 0 K, and reduced life-times Γ's: $\Gamma(T_N)$ at T_N, $\Gamma(T_C)$ at T_C, Γ_0 at 0 K. $E_f = 0.24$ eV, $I = 0.097$ eV and $\tilde{k}_a = 1.8$. See Eq. (20).

	S	$\widetilde{V}$	Δ_0	$\Gamma(T_N)$	$\Gamma(T_C)$	Γ_0
Gd	7/2	–	1.4	–	0.40	0.20
Tb	3	9.3	1.2	0.30	0.29	0.15
Dy	5/2	10.4	1.0	0.25	0.18	0.15
Ho	2	3.3	0.8	0.20	0.10	0.10
Er	3/2	-6.3	0.6			
Tm	1	-12.3	0.4			

As v_1 is estimated to be 3.2×10^{-7} cm/s and the ratio v_2/v_1 is to be about 0.25 from the band calculation of Dy [6], C is estimated to be about 300. Hence at $T = 0$, the spin-wave constant D_1 is estimated to be 0.0125 or 0.0147 eVÅ^{-2} and the maximum magnon-energy $\omega_{\max} = 2SJ_+(0)$ to be 14.1 or 15.7 meV for $\Gamma = 0$ or 0.2, respectively. The experimental values of D_1 and $\omega_{\max}$ are 0.0245 eVÅ^{-2} and 14.3 meV, respectively [10]. A discrepancy between those two values of D_1 should be due to neglect of the other part of Fermi surfaces in the present model. By assuming that the value of Δ is 1.4 or 1.0, and the value of Γ is 0.2 or 0.3 for $T/T_C = 0$ or 0.7, respectively, we can calculate magnon dispersions of ferromagnetic Gd and compare those with the experimental dispersions as shown in Fig. 15 [10]. From the above parameters the characteristic wavenumber $Q_c = 2E_f/v_1$ is estimated to be $0.21[2\pi/c]$, where c is the lattice constant along the c-axis. The anomaly of temperature dependence of the magnon dispersions in the region of $q_z < Q_c$ is explained by the softening of the magnon energies. The reason is that, as mentioned in Ref. [20], decreasing Δ or with increasing temperature, the ferromagnetic state passes near the ferro-cone or ferro-helix boundary (see Fig. 14). Hence we may expect that the softening of the magnon dispersion results in an anomalous decrease of the magnetization [31]. A discrepancy in large q_z region should be due to neglect of effects of other Fermi surfaces, the $\boldsymbol{k}$-dependence of the c-f exchange matrix element I and the zone boundary effect [32].

Secondly we consider the magnon dispersion of Ho in the helical phase. In the helix, the spin-vectors $\langle \boldsymbol{S}_n \rangle$ rotate as their positions $\boldsymbol{R}_n$ advance in the direction of $\boldsymbol{Q}_0$, and are parallel in a particular basal plane perpendicular to the c axis due to the axial crystal-field-anisotropy. Hence the magnon energy at $q_z = Q_0$ becomes finite. Figure 16 shows observed magnon dispersions at 50 K and 78 K [14]. The effect of the axial anisotropy should be introduced to the frequency $\omega(\boldsymbol{q})$ as

$$\omega(\boldsymbol{q}) = \sqrt{[F_1(\boldsymbol{q}) + 2SB]\, F_2(\boldsymbol{q})} \tag{73}$$

where S is the total angular momentum and B the effective axial-anisotropy constant. The constant B is given by (see Appendix D)

$$S^2 B = \frac{3}{2}\overline{V_2^0} - \frac{15}{4}\overline{V_4^0} + \frac{105}{16}\overline{V_6^0}, \tag{74}$$

in which $\overline{V_l^0}$ is the axial-anisotropy constant of the l-th order. From both experimental fit and theoretical fit by assuming the point-charge model, $\overline{V_2^0}$, $\overline{V_4^0}$ and $\overline{V_6^0}$ have been evaluated to be 2.66, 0.414 and -0.539 meV, respectively [1]. The temperature dependence of $\overline{V_n^0}(T)$ is given by the relation

$$\overline{V_n^0}(T) = \overline{V_n^0}\,\sigma^{n(n+1)/2},$$

and the reduced magnetization $\sigma = \langle S \rangle / S$ is derived from the neutron scattering in Ho [33]. By using Eq. (74) and the relation of $\overline{V_n^0}(T)$, the value of B is estimated to be 0.032 meV at 50 K and 0.023 meV at 78 K.

The model-parameters $\tilde{k}_a$ and Δ_0 are assumed to be 1.8 and 0.6, respectively. These values can reproduce the temperature dependence of helical Q_0 [20, 34], but this value of Δ_0 is a little smaller than the value in Table 1. By use of an equation $\Delta/\Delta_0 = \sigma$, Δ is 0.53 at 50 K and 0.4 at 78 K. From the fact that the wavenumber Q_0 approaches 0.27 $[2\pi/c]$ at $T_N = 133$ K, E_f/v_1 is estimated to be 0.14 $[2\pi/c]$. For simplicity we put $\Gamma = 0$.

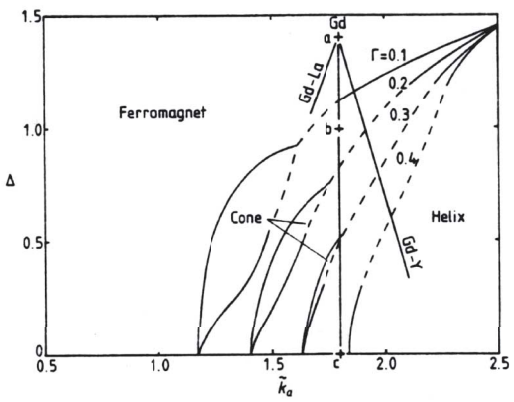

Fig. 14. Phase diagram for $V = 0$ and for some values of Γ; 0.1, 0.2, 0.3 and 0.4 after Ref. [20]. Full curves represent the second-order transition and broken curves the first-order transition. For $\Gamma = 0.4$, the cone region disappears. Vertical line from a to c is an expected temperature-dependence of the Gd state. $\Gamma = 0.2$ for a, 0.3 for b, and 0.4 for c. Full lines denoted by Gd-Y and Gd-La represent the state of the $Gd_{1-x}Y_x$ and $Gd_{1-x}La_x$ alloys at $T = 0$ K, respectively.

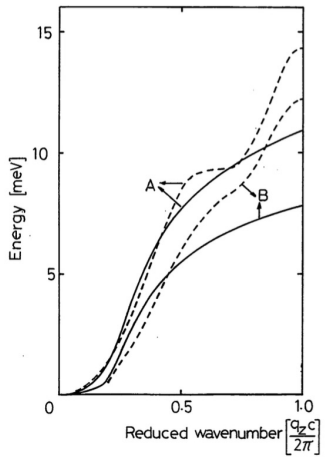

Fig. 15. Magnon dispersions of Gd in the c direction: Curve A at 78 K, and curve B at 232 K; Broken curves by experiment, and full curves by theoretical fitting.

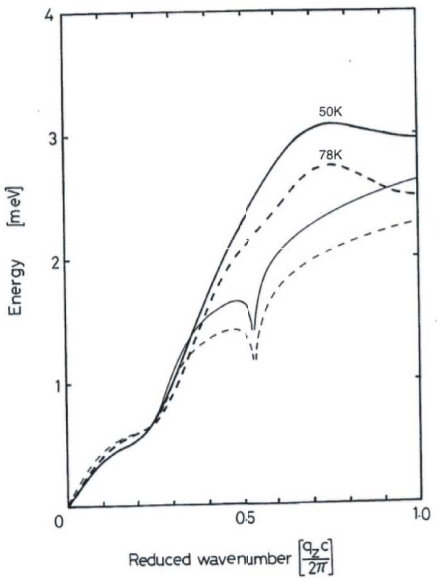

Fig. 16. Magnon dispersions of helical Holmium along the c direction: Full curves at 50 K, and broken curves at 78 K; Thick curves for the experiment and thin curves for the theory.

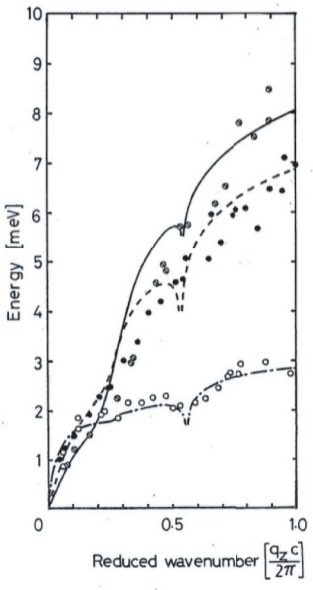

Fig. 17. Magnon dispersions along the c axis of helical phases of Tb_xY_{1-x} alloys at 4.7 K. Experiments: ○, $x = 0.1$; ●, $x = 0.5$; ⊖, $x = 0.76$. Theory: Chain curve, $x = 0.1$; broken curve, $x = 0.5$; full curve, $x = 0.76$.

Table 2. Fitting parameters J_0 and B with values of ± errors for helical Ho.

T [K]	J_0 [meV]	B [meV]
78	$2.54\ ^{+0.31}_{-0.11}$	$0.0369\ ^{-0.0040}_{+0.0017}$
50	$3.02\ ^{+0.31}_{-0.11}$	$0.0346\ ^{-0.0051}_{+0.0067}$

Table 3. Fitting parameters J_0 and B for the magnon dispersions of $Tb_{1-x}Y_x$ alloys.

x	J_0 [meV]	B [meV]
0.1	1.88	0.312
0.5	6.59	0.337
0.75	8.27	0.314

Using the above model parameters and two parameters J_0 and B, we can calculate the magnon dispersion for helical Ho. The parameters J_0 and B are chosen so as to be the mean absolute difference between those two dispersions for $q_z < 0.35\ [2\pi/c]$ less than 0.05 meV. Table 2 gives the values for J_0 and B with the values of errors. Figure 16 shows the comparison between the calculated dispersions and the experimental dispersions [14].

The most prominent feature that the magnon energies for $q_z < Q$ increase with increasing temperature is explained by the temperature dependence of $\Delta = \sigma\Delta_0$, that is, the non-linear effect of the c-f exchange interaction. The effective axial-anisotropy constant in Table 1 is consistent with the values estimated above [1] but its temperature dependence is too weak.

Thirdly let us consider the magnon dispersions in the helical phases of Tb_xY_{1-x} alloys ($0.05 < x < 0.85$) whose moments are confined in the c plane [35] (see Fig. 17). When the mean-field-approximation is applied to those alloys, the magnon dispersion is given by Eq. (73), provided that S is replaced by xS.

For Tb the model parameter $\tilde{k}_a$ is assumed to be 1.8 from Table 1, and Δ_0 to be 1.0 so as to reproduce the x dependence of Q near $T = 0$ K [35]. The life-time Γ is taken to be zero for simplicity. Note that the value of Δ_0 is a little smaller than the value in Table 1 due to the assumption of $\Gamma = 0$. From the fact that the wavenumber of Q_0 approaches 0.28 $[2\pi/c]$ as x tends to zero, E_f/v_1 is estimated to be 0.14 $[2\pi/c]$.

Because the experimental data are so much scattered, we determine two fitting parameters J_0 and B so as to make the calculated magnon-energies provide the fit to the experimental data both at $q_z = Q_0$ and at $q_z = 2\pi/c$. Table 3 shows the values of fitting parameters. The values of B are in good agreement with the value for pure Tb, 0.30 meV, estimated by Kasuya [1]. The values for J_0 do not increase linear but concave as x increases. This fact indicates that the conduction band has not the simplified linear-dispersion of k_z in Eq. (3) but a usual quadratic-dispersion. The reason is that the bottom of the conduction band plays an important role in the case of $\Delta_0 = 1.0$. Note that the same discrepancy is also observed in the temperature dependence of magnon dispersions of helical Ho in Fig. 16. The anomaly of the concentration dependence of the magnon energies which occurs for $q < Q$ described as the feature (c) in Sec. 1 is naturally explained by replacing Δ by $x\Delta_0$, that is, by using the non-linear c-f exchange model as shown in Fig. 17. The calculated dispersions show a softening around $q_z = 0.56$ $[2\pi/d]$ due to the instability of the formation of the second-order harmonic. Actually this instability is observed in the case of $x = 0.1$ while in the other cases smeared by the life-time effect.

Finally, we consider magnon dispersions of conical phase. The most striking feature is that the magnon velocity for $q_z > 0$ is different from one for $q_z < 0$ as shown in

Eq. (61) due to the non-linear c-f exchange effect. The experimental results for $Ho_{0.5}Er_{0.5}$ seems to show this feature [36], but those for Er do not show it [37]. The reason is that Er has large crystal-field anisotropy.

Appendix A. Spin Wave Constant D_1 for Ferromagnet

From the magnon energy

$$\hbar\omega_0(\boldsymbol{q}) = 2S[J_+(\boldsymbol{0}) - J_+(\boldsymbol{q})]$$

and

$$J_+(\boldsymbol{q}) = \frac{I^2}{N}\sum_{\boldsymbol{k}\sigma}\frac{f_{\boldsymbol{k}-\sigma}}{\varepsilon_{\boldsymbol{k}-\boldsymbol{q}\sigma} - \varepsilon_{\boldsymbol{k}-\sigma}},$$

the spin-wave constant along the q_z-direction is

$$D_1 = \frac{1}{2}\frac{\partial^2\omega_0(\boldsymbol{0})}{\partial {q_z}^2} = -S\frac{\partial^2 J_+(\boldsymbol{0})}{\partial {q_z}^2}. \tag{A.1}$$

The second-partial derivative of $J_+(\boldsymbol{q})$ with respect to q_z is given by

$$\frac{\partial^2 J_+(\boldsymbol{q})}{\partial {q_z}^2} = \frac{I^2}{N}\sum_{\boldsymbol{k}\sigma}\frac{f_{\boldsymbol{k}-\sigma}}{(\varepsilon_{\boldsymbol{k}-\boldsymbol{q}\sigma} - \varepsilon_{\boldsymbol{k}-\sigma})^2} \times\left[-\frac{\partial^2\varepsilon_{\boldsymbol{k}-\boldsymbol{q}\sigma}}{\partial {q_z}^2} + \frac{2\,(\partial\varepsilon_{\boldsymbol{k}-\boldsymbol{q}\sigma}/\partial q_z)^2}{\varepsilon_{\boldsymbol{k}-\boldsymbol{q}\sigma} - \varepsilon_{\boldsymbol{k}-\sigma}}\right].$$

Setting $\boldsymbol{q} = \boldsymbol{0}$ and $\varepsilon_{\boldsymbol{k}\sigma} - \varepsilon_{\boldsymbol{k}-\sigma} = -2\sigma IS$, we obtain the formula

$$\frac{\partial^2 J_+(\boldsymbol{0})}{\partial {q_z}^2} = -\frac{1}{4NS^2}\sum_{\boldsymbol{k}\sigma} f_{\boldsymbol{k}-\sigma} \times\left[\frac{\partial^2\varepsilon_{\boldsymbol{k}}}{\partial {k_z}^2} - \frac{\sigma}{IS}\left(\frac{\partial\varepsilon_{\boldsymbol{k}}}{\partial k_z}\right)^2\right]. \tag{A.2}$$

Using the band model of Eq. (3), we have

$$\frac{\partial\varepsilon_{\boldsymbol{k}}}{\partial k_z} = -v_1\,\mathrm{sgn}\,k_z, \quad \frac{\partial^2\varepsilon_{\boldsymbol{k}}}{\partial {k_z}^2} = 2v_1\,\delta(k_z)\,, \tag{A.3}$$

where sgn is the sign function, and hence the simpler formula

$$D_1 = \frac{v_1}{2NS}\sum_{\boldsymbol{k}\sigma} f_{\boldsymbol{k}\sigma}\left[\delta(k_z) - \frac{\sigma\,v_1}{2IS}\right]. \tag{A.4}$$

Note that $f_{\boldsymbol{k}\downarrow} = 0$ for $\Delta > 1$.

Appendix B. The f-f Exchange Matrix Elements $\mathcal{J}_{ij}(\boldsymbol{q})$

$\mathcal{J}_{ij}(\boldsymbol{q})$ is represented as

$$\mathcal{J}_{ij}(\boldsymbol{q}) = K_{ij}(\boldsymbol{q})(1 - \delta_{\boldsymbol{q},\boldsymbol{0}}) + J_{ij}(\boldsymbol{q}). \tag{B.1}$$

where $\delta_{\boldsymbol{q},\boldsymbol{0}}$ is a Kronecker's delta. $K_{ij}(\boldsymbol{q})$ and $J_{ij}(\boldsymbol{q})$ are given as follows,

$$\begin{pmatrix} K_{11}(\boldsymbol{q}) & K_{12}(\boldsymbol{q}) & K_{13}(\boldsymbol{q}) \\ & K_{22}(\boldsymbol{q}) & K_{23}(\boldsymbol{q}) \\ & & K_{33}(\boldsymbol{q}) \end{pmatrix} = \frac{I^2}{N}\sum_{\boldsymbol{k}\mu}\frac{f_{\boldsymbol{k}\mu}(1 - f_{\boldsymbol{k}'\mu})}{E_{\boldsymbol{k}'\mu} - E_{\boldsymbol{k}\mu}} \times\begin{pmatrix} s^2(\alpha) & \mu\; s(\alpha)s(\beta) & s(\alpha)c(\alpha) \\ & s^2(\beta) & -\mu\; s(\beta)c(\alpha) \\ & & c^2(\alpha) \end{pmatrix}$$

and

$$\begin{pmatrix} J_{11}(\boldsymbol{q}) & J_{12}(\boldsymbol{q}) & J_{13}(\boldsymbol{q}) \\ & J_{22}(\boldsymbol{q}) & J_{23}(\boldsymbol{q}) \\ & & J_{33}(\boldsymbol{q}) \end{pmatrix} = \frac{I^2}{N}\sum_{\boldsymbol{k}\mu}\frac{f_{\boldsymbol{k}\mu}(1 - f_{\boldsymbol{k}'-\mu})}{E_{\boldsymbol{k}'-\mu} - E_{\boldsymbol{k}\mu}} \times\begin{pmatrix} c^2(\alpha) & -\mu\; c(\alpha)c(\beta) & -c(\alpha)s(\alpha) \\ & c^2(\beta) & -\mu\; c(\beta)s(\alpha) \\ & & s^2(\alpha) \end{pmatrix}$$

where $\boldsymbol{k}' = \boldsymbol{k} - \boldsymbol{q}$, $\alpha = \theta_{\boldsymbol{k}} + \theta_{\boldsymbol{k}'} - \theta$, $\beta = \theta_{\boldsymbol{k}} - \theta_{\boldsymbol{k}'}$, $c(\theta) = \cos\theta$ and $s(\theta) = \sin\theta$. Note that in the limit of $\boldsymbol{q} = \boldsymbol{0}$, $K_{22}(\boldsymbol{q})$ becomes zero so that $\mathcal{J}_{22}(\boldsymbol{q})$ is continuous at $\boldsymbol{q} = \boldsymbol{0}$.

Appendix C. The Proof of Equations (56), (57), (58), (59), (60) and (40)

In the following we denote $\boldsymbol{Q}_0$ and θ_0 by $\boldsymbol{Q}$ and θ for convenience. From Eqs. (46), (50), (55) and (B.1), we have for $i = 1, 2$

$$\begin{aligned} F_i(\boldsymbol{q}) &= \mathcal{J}_0 - 2S\mathcal{J}^+_{jj}(\boldsymbol{q}), \\ \mathcal{J}^+_{ii}(\boldsymbol{q}) &= K^+_{ii}(\boldsymbol{q})(1 - \delta_{\boldsymbol{q},\boldsymbol{0}}) + J^+_{ii}(-\boldsymbol{q}), \\ K^+_{ii}(\boldsymbol{q}) &= \frac{1}{2}[K_{ii}(\boldsymbol{q}) + K_{ii}(-\boldsymbol{q})], \\ J^+_{ii}(\boldsymbol{q}) &= \frac{1}{2}[J_{ii}(\boldsymbol{q}) + J_{ii}(-\boldsymbol{q})], \\ \mathcal{J}_0 &= \frac{I}{N}\sum_{\boldsymbol{k}}(f_{\boldsymbol{k}-} - f_{\boldsymbol{k}+})\cos(2\theta_{\boldsymbol{k}} - \theta), \end{aligned}$$

where $f_{\boldsymbol{k}\mu} = f(E_{\boldsymbol{k}\mu})$. For simplicity we use the following abbrebiations

$$\left.\begin{aligned} \varepsilon_0 &= \varepsilon_{\boldsymbol{k}}, \quad \varepsilon_\pm = \varepsilon_{\boldsymbol{k}\pm\boldsymbol{Q}}, \quad D = IS, \\ R_- &= \sqrt{(\varepsilon_- - \varepsilon_0 + 2y)^2 + 4x^2}, \\ R_+ &= \sqrt{(\varepsilon_0 - \varepsilon_+ + 2y)^2 + 4x^2}, \\ P_\pm &= 4D^2 + 2y(\varepsilon_- - \varepsilon_+) \\ &\quad \pm(\varepsilon_- - \varepsilon_0)(\varepsilon_0 - \varepsilon_+). \end{aligned}\right\} \tag{C.1}$$

Then from Eq. (9), we have

$$\left.\begin{aligned} \sin 2\theta_{\boldsymbol{k}} &= \tfrac{2x}{R_-}, \quad \cos 2\theta_{\boldsymbol{k}} = \tfrac{\varepsilon_- - \varepsilon_0 + 2y}{R_-}, \\ \sin(2\theta_{\boldsymbol{k}} - \theta) &= -\tfrac{(\varepsilon_- - \varepsilon_0)\sin\theta}{R_-}, \\ \cos(2\theta_{\boldsymbol{k}} - \theta) &= \tfrac{(\varepsilon_- - \varepsilon_0)\cos\theta + 2D}{R_-}. \end{aligned}\right\} \tag{C.2}$$

(1) The proof of Eq. (56)

The Fourier transforms of the f-spin operators $S_{\boldsymbol{q}\xi}$ and $S_{\boldsymbol{q}\eta}$ are

$$\left.\begin{aligned} S_{\boldsymbol{q}\xi} &= \tfrac{1}{\sqrt{N}}\textstyle\sum_n \mathrm{e}^{-\mathrm{i}\,\boldsymbol{q}\cdot\boldsymbol{R}_n} S_{n\xi}, \\ S_{\boldsymbol{q}\eta} &= \tfrac{1}{\sqrt{N}}\textstyle\sum_n \mathrm{e}^{-\mathrm{i}\,\boldsymbol{q}\cdot\boldsymbol{R}_n} S_{n\eta}. \end{aligned}\right\} \tag{C.3}$$

Defining the f-spin operators as

$$S_{n\pm} = S_{n\xi} \pm \mathrm{i}S_{n\eta}, \quad S_{n0} = S_{n\zeta} - S,$$

and using the same relations as Eqs. (34) and (35), we obtain

$$\left.\begin{aligned} S_{\boldsymbol{q}\xi} &\simeq \sqrt{S/2}(b_{\boldsymbol{q}} + b^\dagger_{\boldsymbol{q}}), \\ \mathrm{i}S_{\boldsymbol{q}\eta} &\simeq \sqrt{S/2}(b_{\boldsymbol{q}} - b^\dagger_{\boldsymbol{q}}). \end{aligned}\right\} \tag{C.4}$$

From Eq. (51) we have

$$\left.\begin{aligned}\beta_{\boldsymbol{q}} &= b_{\boldsymbol{q}}\cosh\phi_{\boldsymbol{q}} + b^{\dagger}_{-\boldsymbol{q}}\sinh\phi_{\boldsymbol{q}},\\ \beta^{\dagger}_{-\boldsymbol{q}} &= b^{\dagger}_{-\boldsymbol{q}}\cosh\phi_{\boldsymbol{q}} + b_{\boldsymbol{q}}\sinh\phi_{\boldsymbol{q}},\end{aligned}\right\}$$

and hence

$$\left.\begin{aligned}\beta_{\boldsymbol{q}} + \beta^{\dagger}_{-\boldsymbol{q}} &= \mathrm{e}^{\phi_{\boldsymbol{q}}}(b_{\boldsymbol{q}} + b^{\dagger}_{-\boldsymbol{q}}),\\ \beta_{\boldsymbol{q}} - \beta^{\dagger}_{-\boldsymbol{q}} &= \mathrm{e}^{-\phi_{\boldsymbol{q}}}(b_{\boldsymbol{q}} - b^{\dagger}_{-\boldsymbol{q}}).\end{aligned}\right\} \tag{C.5}$$

From Eqs. (52) and (55) we have

$$\mathrm{e}^{\phi_{\boldsymbol{q}}} = \sqrt{F_1(\boldsymbol{q})/F_2(\boldsymbol{q})}. \tag{C.6}$$

Using Eqs. (C.5) and (C.6) we can rewrite Eq. (C.4) as

$$\left.\begin{aligned}S_{\boldsymbol{q}\xi} &\simeq \sqrt{\tfrac{S}{2}}\left[\tfrac{F_2(\boldsymbol{q})}{F_1(\boldsymbol{q})}\right]^{1/4}(\beta_{\boldsymbol{q}} + \beta^{\dagger}_{-\boldsymbol{q}}),\\ \mathrm{i}S_{\boldsymbol{q}\eta} &\simeq \sqrt{\tfrac{S}{2}}\left[\tfrac{F_1(\boldsymbol{q})}{F_2(\boldsymbol{q})}\right]^{1/4}(\beta_{\boldsymbol{q}} - \beta^{\dagger}_{-\boldsymbol{q}}).\end{aligned}\right\} \tag{C.7}$$

(2) The proof of Eq. (57)

From Appendix B,

$$\left.\begin{aligned}K^{+}_{22}(\boldsymbol{q}) &= \tfrac{I^2}{2N}\textstyle\sum_{\boldsymbol{k}\mu}\frac{f_{\boldsymbol{k}\mu} - f_{\boldsymbol{k}'\mu}}{E_{\boldsymbol{k}'\mu} - E_{\boldsymbol{k}\mu}}\sin^2\beta,\\ J^{+}_{22}(\boldsymbol{q}) &= \tfrac{I^2}{2N}\textstyle\sum_{\boldsymbol{k}\mu}\frac{f_{\boldsymbol{k}\mu} - f_{\boldsymbol{k}'-\mu}}{E_{\boldsymbol{k}'-\mu} - E_{\boldsymbol{k}\mu}}\cos^2\beta,\end{aligned}\right\} \tag{C.8}$$

where $\boldsymbol{k}' = \boldsymbol{k} - \boldsymbol{q}$ and $\beta = \theta_{\boldsymbol{k}} - \theta_{\boldsymbol{k}'}$. Letting $\boldsymbol{q}$ go to zero, we have

$$K^{+}_{22}(\boldsymbol{0}^{+}) = \lim_{\boldsymbol{q}\to\boldsymbol{0}} K^{+}_{22}(\boldsymbol{q}) = 0, \tag{C.9}$$

and in the same notation of $\boldsymbol{0}^{+}$ as $\boldsymbol{q}\to\boldsymbol{0}$

$$J^{+}_{22}(\boldsymbol{0}^{+}) = \frac{I^2}{N}\sum_{\boldsymbol{k}\mu}\frac{f_{\boldsymbol{k}-} - f_{\boldsymbol{k}+}}{R_-}. \tag{C.10}$$

From Eq. (C.2), we have

$$\cos(2\theta_{\boldsymbol{k}} - \theta) = \frac{2D}{R_-} - \cot\theta\sin(2\theta_{\boldsymbol{k}} - \theta). \tag{C.11}$$

Using the partial derivative of $E_{\boldsymbol{k}\mu}$

$$\frac{\partial E_{\boldsymbol{k}\mu}}{\partial\theta} = \mu D\sin(2\theta_{\boldsymbol{k}} - \theta), \tag{C.12}$$

we can rewrite Eq. (17) as

$$\frac{\partial\mathcal{E}_0}{\partial\theta} = -D\sum_{\boldsymbol{k}}(f_{\boldsymbol{k}-} - f_{\boldsymbol{k}+})\sin(2\theta_{\boldsymbol{k}} - \theta). \tag{C.13}$$

Putting Eq. (C.11) into the above expression of $\mathcal{J}_0$ and using Eqs. (C.8), (C.10) and (C.13), we can rewrite $\mathcal{J}_0$ as

$$\mathcal{J}_0 = 2S\mathcal{J}^{+}_{22}(\boldsymbol{0}^{+}) - \frac{\cot\theta}{NS}\frac{\partial\mathcal{E}_0}{\partial\theta}. \tag{C.14}$$

Hence we obtain

$$F_2(\boldsymbol{0}^{+}) = \mathcal{J}_0 - 2S\mathcal{J}^{+}_{22}(\boldsymbol{0}^{+}) = -\frac{\cot\theta}{NS}\frac{\partial\mathcal{E}_0}{\partial\theta}. \tag{C.15}$$

In the equilibrium state, the partial derivative $\partial\mathcal{E}_0/\partial\theta = 0$ and hence

$$F_2(\boldsymbol{0}^{+}) = -\frac{\cot\theta_0}{NS}\frac{\partial}{\partial\theta}\mathcal{E}_0(\theta_0, \boldsymbol{Q}_0) = 0. \tag{C.16}$$

(3) The proof of Eq. (58)

From Appendix B,

$$\left.\begin{aligned}K^{+}_{11}(\boldsymbol{q}) &= \tfrac{I^2}{2N}\textstyle\sum_{\boldsymbol{k}\mu}\frac{f_{\boldsymbol{k}\mu} - f_{\boldsymbol{k}'\mu}}{E_{\boldsymbol{k}'\mu} - E_{\boldsymbol{k}\mu}}\sin^2\alpha,\\ J^{+}_{11}(\boldsymbol{q}) &= \tfrac{I^2}{2N}\textstyle\sum_{\boldsymbol{k}\mu}\frac{f_{\boldsymbol{k}\mu} - f_{\boldsymbol{k}'-\mu}}{E_{\boldsymbol{k}'-\mu} - E_{\boldsymbol{k}\mu}}\cos^2\alpha,\end{aligned}\right\} \tag{C.17}$$

where $\boldsymbol{k}' = \boldsymbol{k} - \boldsymbol{q}$ and $\alpha = \theta_{\boldsymbol{k}} + \theta_{\boldsymbol{k}'} - \theta$. Letting $\boldsymbol{q}$ go to zero, we have

$$\left.\begin{aligned}K^{+}_{11}(\boldsymbol{0}^{+}) &= -\tfrac{I^2}{2N}\textstyle\sum_{\boldsymbol{k}\mu}\frac{\partial f_{\boldsymbol{k}\mu}}{\partial E_{\boldsymbol{k}\mu}}\sin^2(2\theta_{\boldsymbol{k}} - \theta),\\ J^{+}_{11}(\boldsymbol{0}^{+}) &= \tfrac{I^2}{N}\textstyle\sum_{\boldsymbol{k}}\frac{f_{\boldsymbol{k}-} - f_{\boldsymbol{k}+}}{R_-}\cos^2(2\theta_{\boldsymbol{k}} - \theta).\end{aligned}\right\} \tag{C.18}$$

The second derivative of $\mathcal{E}_0$ is

$$\frac{\partial^2\mathcal{E}_0}{\partial\theta^2} = \sum_{\boldsymbol{k}\mu}\left[\frac{\partial^2 E_{\boldsymbol{k}\mu}}{\partial\theta^2}f_{\boldsymbol{k}\mu} + \left(\frac{\partial E_{\boldsymbol{k}\mu}}{\partial\theta}\right)^2\frac{\partial f_{\boldsymbol{k}\mu}}{\partial\theta}\right]. \tag{C.19}$$

From Eq. (C.12) we have

$$\begin{aligned}\frac{\partial^2 E_{\boldsymbol{k}\mu}}{\partial\theta^2} &= -\mu D\cos(2\theta_{\boldsymbol{k}} - \theta)\\ &\times\left(1 - \frac{2D}{R_-}\cos(2\theta_{\boldsymbol{k}} - \theta)\right).\end{aligned} \tag{C.20}$$

Using Eq. (C.18) with Eqs. (C.14) and (C.20) we rewrite the first and second terms of Eq. (C.19) as

$$\sum_{\boldsymbol{k}\mu}\frac{\partial^2 E_{\boldsymbol{k}\mu}}{\partial\theta^2}f_{\boldsymbol{k}\mu} = NS\left\{\mathcal{J}_0 - 2SJ^{+}_{11}(\boldsymbol{0}^{+})\right\},$$

$$\sum_{\boldsymbol{k}\mu}\left(\frac{\partial E_{\boldsymbol{k}\mu}}{\partial\theta}\right)^2\frac{\partial f_{\boldsymbol{k}\mu}}{\partial E_{\boldsymbol{k}\mu}} = -2NS^2K^{+}_{11}(\boldsymbol{0}^{+}).$$

Hence using Eqs. (C.19) and (55) and $\mathcal{J}^{+}_{ii}(\boldsymbol{q}) = J^{+}_{ii}(\boldsymbol{q}) + K^{+}_{ii}(\boldsymbol{q})$, we obtain

$$\frac{1}{NS}\frac{\partial^2\mathcal{E}_0}{\partial\theta^2} = \mathcal{J}_0 - 2S\mathcal{J}^{+}_{11}(\boldsymbol{0}^{+}) = F_1(\boldsymbol{0}^{+}). \tag{C.21}$$

(4) The proof of Eq. (59)

From Eqs. (C.2), we have

$$\left.\begin{aligned}\sin^2\alpha &= \tfrac{R_-R_+ - P_- + 2c^2(\varepsilon_- - \varepsilon_0)(\varepsilon_0 - \varepsilon_+)}{2R_-R_+},\\ \cos^2\alpha &= \tfrac{R_-R_+ + P_- + 2c^2(\varepsilon_- - \varepsilon_0)(\varepsilon_0 - \varepsilon_+)}{2R_-R_+},\\ \sin^2\beta &= \tfrac{R_-R_+ - P_+}{2R_-R_+},\\ \cos^2\beta &= \tfrac{R_-R_+ + P_+}{2R_-R_+},\\ E_{\boldsymbol{k}'\pm} - E_{\boldsymbol{k}\pm} &= \tfrac{R_-R_+ - P_-}{\varepsilon_+ - \varepsilon_- \mp (R_-R_+)},\\ E_{\boldsymbol{k}'\mp} - E_{\boldsymbol{k}\pm} &= -\tfrac{R_-R_+ + P_-}{\varepsilon_+ - \varepsilon_- \pm (R_+R_+)},\end{aligned}\right\} \tag{C.22}$$

where $\boldsymbol{k}' = \boldsymbol{k} + \boldsymbol{Q}$ and $\alpha = \theta_{\boldsymbol{k}} + \theta_{\boldsymbol{k}'} - \theta$ and $\beta = \theta_{\boldsymbol{k}'} - \theta_{\boldsymbol{k}}$. Using Eq. (C.22) we can derive the following equations

$$\begin{aligned}\frac{\sin^2\alpha}{E_{\boldsymbol{k}'\mu} - E_{\boldsymbol{k}\mu}} &= \frac{\varepsilon_+ - \varepsilon_- - \mu(R_+ - R_-)}{2R_-R_+}\\ &- \frac{\cos^2\theta(\varepsilon_- - \varepsilon_0)(\varepsilon_0 - \varepsilon_+)}{R_-R_+(E_{\boldsymbol{k}'\mu} - E_{\boldsymbol{k}\mu})},\end{aligned} \tag{C.23}$$

$$\begin{aligned}\frac{\cos^2\alpha}{E_{\boldsymbol{k}'-\mu} - E_{\boldsymbol{k}\mu}} &= -\frac{\varepsilon_+ - \varepsilon_- + \mu(R_+ + R_-)}{2R_-R_+}\\ &+ \frac{\cos^2\theta(\varepsilon_- - \varepsilon_0)(\varepsilon_0 - \varepsilon_+)}{R_-R_+(E_{\boldsymbol{k}'-\mu} - E_{\boldsymbol{k}\mu})},\end{aligned} \tag{C.24}$$

$$\frac{\sin^2\beta}{E_{\boldsymbol{k}'\mu}-E_{\boldsymbol{k}\mu}}=\frac{\varepsilon_+-\varepsilon_--\mu(R_+-R_-)}{2R_-R_+} -\frac{(\varepsilon_--\varepsilon_0)(\varepsilon_0-\varepsilon_+)}{R_-R_+(E_{\boldsymbol{k}'\mu}-E_{\boldsymbol{k}\mu})}, \tag{C.25}$$

$$\frac{\cos^2\beta}{E_{\boldsymbol{k}'-\mu}-E_{\boldsymbol{k}\mu}}=-\frac{\varepsilon_+-\varepsilon_-+\mu(R_++R_-)}{2R_-R_+} +\frac{(\varepsilon_--\varepsilon_0)(\varepsilon_0-\varepsilon_+)}{R_-R_+(E_{\boldsymbol{k}'-\mu}-E_{\boldsymbol{k}\mu})}. \tag{C.26}$$

Using Eqs. (C.23) and (C.24), we can rewrite $\mathcal{J}_{11}(\boldsymbol{Q})$ as

$$\begin{aligned}\mathcal{J}_{11}^+(\boldsymbol{Q})&=K_{11}^+(\boldsymbol{Q})+J_{11}^+(\boldsymbol{Q})\\&=\frac{I^2}{N}\sum_{\boldsymbol{k}}\frac{f_{\boldsymbol{k}-}-f_{\boldsymbol{k}+}}{R_-}\\&-\cos^2\theta\frac{I^2}{2N}\sum_{\boldsymbol{k}\mu}\frac{(\varepsilon_--\varepsilon_0)(\varepsilon_0-\varepsilon_+)}{R_-R_+}\\&\times\left(\frac{f_{\boldsymbol{k}\mu}-f_{\boldsymbol{k}'\mu}}{E_{\boldsymbol{k}'\mu}-E_{\boldsymbol{k}\mu}}-\frac{f_{\boldsymbol{k}\mu}-f_{\boldsymbol{k}'-\mu}}{E_{\boldsymbol{k}'-\mu}-E_{\boldsymbol{k}\mu}}\right).\end{aligned} \tag{C.27}$$

Using Eqs. (C.25) and (C.26), we can rewrite $\mathcal{J}_{22}(\boldsymbol{Q})$ as

$$\begin{aligned}\mathcal{J}_{22}^+(\boldsymbol{Q})&=K_{22}^+(\boldsymbol{Q})+J_{22}^+(\boldsymbol{Q})\\&=\frac{I^2}{N}\sum_{\boldsymbol{k}}\frac{f_{\boldsymbol{k}-}-f_{\boldsymbol{k}+}}{R_-}\\&-\frac{I^2}{2N}\sum_{\boldsymbol{k}\mu}\frac{(\varepsilon_--\varepsilon_0)(\varepsilon_0-\varepsilon_+)}{R_-R_+}\\&\times\left(\frac{f_{\boldsymbol{k}\mu}-f_{\boldsymbol{k}'\mu}}{E_{\boldsymbol{k}'\mu}-E_{\boldsymbol{k}\mu}}-\frac{f_{\boldsymbol{k}\mu}-f_{\boldsymbol{k}'-\mu}}{E_{\boldsymbol{k}'-\mu}-E_{\boldsymbol{k}\mu}}\right).\end{aligned} \tag{C.28}$$

From Eqs. (B.1) , (C.9) and (C.10) the first term of LHS of Eqs. (C.27) and (C.28) is given by $\mathcal{J}_{22}^+(\boldsymbol{0}^+)$. In the equilibrium state, from Eq. (C.14) we have $\mathcal{J}_{22}^+(\boldsymbol{0}^+)=\mathcal{J}_0$ and hence

$$\mathcal{J}_0-\mathcal{J}_{11}^+(\boldsymbol{Q})=\cos^2\theta\left(\mathcal{J}_0-\mathcal{J}_{22}^+(\boldsymbol{Q})\right). \tag{C.29}$$

Finally we obtain

$$F_1(\boldsymbol{Q})=\cos^2\theta\ F_2(\boldsymbol{Q}). \tag{C.30}$$

(5) The proof of Eq. (60)

The f-spin operator $\boldsymbol{S}_n$ is defined by

$$\boldsymbol{S}_n=(S_{nx},S_{ny},S_{nz}).$$

From Eq. (7) we have

$$\left.\begin{aligned}S_{nx}&=S_{n\xi}\cos\theta\cos\phi_n-S_{n\eta}\sin\phi_n\\&\quad+S_{n\zeta}\sin\theta\cos\phi_n,\\S_{ny}&=S_{n\xi}\cos\theta\sin\phi_n+S_{n\eta}\cos\phi_n\\&\quad+S_{n\zeta}\sin\theta\sin\phi_n,\\S_{nz}&=-S_{n\xi}\sin\theta+S_{n\zeta}\cos\theta.\end{aligned}\right\} \tag{C.31}$$

By using Eqs. (C.31), (C.3) and $\phi_n=\boldsymbol{Q}\cdot\boldsymbol{R}_n$, we rewrite S^- as

$$\begin{aligned}S^-&=\sum_n(S_{nx}-\mathrm{i}S_{ny})\\&=\sqrt{N}\left(S_{\boldsymbol{Q}\xi}\cos\theta-\mathrm{i}S_{\boldsymbol{Q}\eta}+S_{\boldsymbol{Q}\zeta}\sin\theta\right)\mathrm{e}^{-\mathrm{i}\phi_n}.\end{aligned}$$

From Eqs. (C.7) and (C.30), we have

$$\left.\begin{aligned}S_{\pm\boldsymbol{Q}\xi}&\simeq\sqrt{\tfrac{S}{2\cos\theta}}(\beta_{\pm\boldsymbol{Q}}+\beta_{\mp\boldsymbol{Q}}^\dagger),\\\mathrm{i}S_{\pm\boldsymbol{Q}\eta}&\simeq\sqrt{\tfrac{S\cos\theta}{2}}\ (\beta_{\pm\boldsymbol{Q}}-\beta_{\mp\boldsymbol{Q}}^\dagger).\end{aligned}\right\} \tag{C.32}$$

Hence we obatain

$$S^-\simeq(NS\sin\theta)\ \delta_{\boldsymbol{Q},\boldsymbol{0}}+\sqrt{2NS\cos\theta}\ \beta_{-\boldsymbol{Q}}^\dagger. \tag{C.33}$$

(6) The mode of oscillation for $q=\pm Q$

We consider the two modes of oscillations corresponding to $\omega(\boldsymbol{Q})$ and $\omega(-\boldsymbol{Q})$. The classical picture is represented here [4]. For $\omega_-=\omega(-\boldsymbol{Q})$, let us put $\beta_{\boldsymbol{Q}}=\beta_{\boldsymbol{Q}}^\dagger=0$, $\beta_{-\boldsymbol{Q}}=|\beta|\exp(-\mathrm{i}\omega_-t+\psi)$ and $\beta_{-\boldsymbol{Q}}^\dagger=|\beta|\exp(\mathrm{i}\omega_-t-\psi)$ where ψ is an arbitrary phase. Hence we obtain

$$\left.\begin{aligned}S_{n\xi}&=\sqrt{\tfrac{2S}{N\cos\theta}}|\beta|\cos(-\phi_n-\omega_-t+\psi),\\S_{n\eta}&=\sqrt{\tfrac{2S\cos\theta}{N}}|\beta|\sin(-\phi_n-\omega_-t+\psi).\end{aligned}\right\} \tag{C.34}$$

Using Eqs. (C.31) and (C.34) and setting $\psi=\omega_-t$ for example, we have

$$\left.\begin{aligned}S_{nx}&\simeq S\sin\theta\cos\phi_n+A\cos\theta,\\S_{ny}&\simeq S\sin\theta\sin\phi_n,\\S_{nz}&\simeq S\cos\theta-A\sin\theta\cos\phi_n,\end{aligned}\right\} \tag{C.35}$$

where the amplitude A is given by $\sqrt{2S/N\cos\theta}|\beta|$. Hence we obtain

$$\boldsymbol{S}_n\simeq\langle\boldsymbol{S}_n\rangle+A\langle S\rangle^{-1}\langle\boldsymbol{S}_n\rangle\times\boldsymbol{e}_y, \tag{C.36}$$

where $\langle S\rangle$ is equal to S at $T=0$. The mode of oscillation is such that the whole spin system rotates as a rigid body about the y-axis on the plane perpendicular to the cone axis. Hence $\omega(-\boldsymbol{Q})=0$. This situation can be seen from Eq. (C.33) [27].

For $\omega(\boldsymbol{Q})$, let us put $\beta_{-\boldsymbol{Q}}=\beta_{-\boldsymbol{Q}}^\dagger=0$, $\beta_{\boldsymbol{Q}}=|\beta|\exp(-\mathrm{i}\omega_-t+\psi)$ and $\beta_{\boldsymbol{Q}}^\dagger=|\beta|\exp(\mathrm{i}\omega_-t-\psi)$. In the same calculation, we obtain

$$\left.\begin{aligned}S_{nx}&\simeq S\sin\theta\cos\phi_n+A\cos\theta\cos2\phi_n,\\S_{ny}&\simeq S\sin\theta\sin\phi_n+A\cos\theta\sin2\phi_n,\\S_{nz}&\simeq S\cos\theta-A\sin\theta\cos\phi_n.\end{aligned}\right\} \tag{C.37}$$

This motion of the cone includes a bending oscillation of the cone surface.

(7) The proof of Eq. (40)

If the cone angle θ goes to zero under the condition of Eq. (19)

$$|Q/Q_f-1|\le 2D\sin\theta/E_f,$$

then $x\to0$, $y\to D$, $Q\to Q_f$ and

$$\left.\begin{aligned}&\cos(2\theta_{\boldsymbol{k}}-\theta)\to\mathrm{sgn}(\varepsilon_{\boldsymbol{k}-\boldsymbol{Q}\downarrow}-\varepsilon_{\boldsymbol{k}\uparrow}),\\&\sin(2\theta_{\boldsymbol{k}}-\theta)\to0.\end{aligned}\right\} \tag{C.38}$$

Using Eq. (C.38) and the following relations

$$E_{\boldsymbol{k}+}\to\begin{cases}\varepsilon_{\boldsymbol{k}-\boldsymbol{Q}\downarrow}, & \text{for } \varepsilon_{\boldsymbol{k}-\boldsymbol{Q}\downarrow}>\varepsilon_{\boldsymbol{k}\uparrow},\\ \varepsilon_{\boldsymbol{k}\uparrow}, & \text{for } \varepsilon_{\boldsymbol{k}-\boldsymbol{Q}\downarrow}<\varepsilon_{\boldsymbol{k}\uparrow},\end{cases}$$

$$E_{\boldsymbol{k}-} \to \begin{cases} \varepsilon_{\boldsymbol{k}\uparrow} & , \quad \text{for } \varepsilon_{\boldsymbol{k}-\boldsymbol{Q}\downarrow} > \varepsilon_{\boldsymbol{k}\uparrow}, \\ \varepsilon_{\boldsymbol{k}-\boldsymbol{Q}\downarrow} & , \quad \text{for } \varepsilon_{\boldsymbol{k}-\boldsymbol{Q}\downarrow} < \varepsilon_{\boldsymbol{k}\uparrow}, \end{cases}$$

we obtain from Eqs. (30) and (32)

$$\begin{aligned} \mathcal{J}_0 &\to \frac{I}{N}\sum_{\boldsymbol{k}}(f_{\boldsymbol{k}-} - f_{\boldsymbol{k}+})\,\mathrm{sgn}(\varepsilon_{\boldsymbol{k}-\boldsymbol{Q}\downarrow} - \varepsilon_{\boldsymbol{k}\uparrow}), \\ &= \frac{I}{N}\sum_{\boldsymbol{k}}(f_{\boldsymbol{k}\uparrow} - f_{\boldsymbol{k}\downarrow}) = 2SJ_+(\boldsymbol{0}). \end{aligned} \tag{C.39}$$

On the other hand, as θ goes to zero, from Eq. (C.17) we have

$$K_{11}^{+}(\boldsymbol{0}^+) \to 0,$$

$$\begin{aligned} J_{11}^{+}(\boldsymbol{0}^+) &\to \frac{I^2}{N}\sum_{\boldsymbol{k}}\frac{f_{\boldsymbol{k}-} - f_{\boldsymbol{k}+}}{E_{\boldsymbol{k}+} - E_{\boldsymbol{k}-}} \\ &= \frac{I^2}{N}\sum_{\boldsymbol{k}}\frac{f_{\boldsymbol{k}\uparrow} - f_{\boldsymbol{k}\downarrow}}{E_{\boldsymbol{k}\uparrow} - E_{\boldsymbol{k}\downarrow}} = J_+(\boldsymbol{Q}_f), \end{aligned}$$

and hence

$$\mathcal{J}_{11}^{+}(\boldsymbol{0}^+) \to J_+(\boldsymbol{Q}_f). \tag{C.40}$$

From Eqs. (C.39) and (C.40), we obtain

$$\begin{aligned} F_1(\boldsymbol{0}^+) &= \mathcal{J}_0 - 2S\mathcal{J}_{11}^{+}(\boldsymbol{0}^+) \\ &\to 2S[J_+(\boldsymbol{0}) - J_+(\boldsymbol{Q}_f)] = \omega_0(\boldsymbol{Q}_f). \end{aligned} \tag{C.41}$$

Appendix D. The Effective Anisotropy Constant B

In the rare earth metals with the hexagonal closed packed structure, there are the second, the fourth and the sixth order anisotropy field. Neglecting the planner anisotropy for the simple helix or the cone structure given by Eq. (5), we write the crystal field anisotropy as

$$\begin{aligned} H_{cry} = \sum_n [&\overline{V_2^{\,0}}\, O_2^{\,0}(\boldsymbol{S}_n) \\ &+\overline{V_4^{\,0}}\, O_4^{\,0}(\boldsymbol{S}_n) + \overline{V_6^{\,0}}\, O_6^{\,0}(\boldsymbol{S}_n)] \end{aligned} \tag{D.1}$$

where $O_k^{\,0}(\boldsymbol{S}_n)$ is the Racah operator and $\boldsymbol{S}_n = (S_{nx}, S_{ny}, S_{nz})$. Rewriting Eq. (D.1) in terms of the local f spin operator $(S_{n\xi}, S_{n\eta}, S_{n\zeta})$ and using the Bose-operator expansion of the Racah operator [38], we obtain

$$\begin{aligned} H_{cry} &= \mathcal{E}_{cry} + h(a_0 + a_0^{\dagger}) \\ &+ \sum_{\boldsymbol{q}}[K_1 a_{\boldsymbol{q}}^{\dagger}\, a_{\boldsymbol{q}} + \frac{1}{2}K_2(a_{\boldsymbol{q}}^{\dagger}\, a_{-\boldsymbol{q}}^{\dagger} + a_{\boldsymbol{q}}\, a_{-\boldsymbol{q}})] \end{aligned} \tag{D.2}$$

where

$$\begin{aligned} \mathcal{E}_{cry} &= N(\overline{V_2^{\,0}}\, P_2^{\,0} + \overline{V_4^{\,0}}\, P_4^{\,0} + \overline{V_6^{\,0}}\, P_6^{\,0}), \\ h &= \frac{N}{2S}(\overline{V_2^{\,0}}\, P_2^{\,1} + \overline{V_4^{\,0}}\, P_4^{\,1} + \overline{V_6^{\,0}} P_6^{\,1}), \\ K_1 &= -\frac{1}{S}(3\overline{V_2^{\,0}}\, P_2^{\,0} + 10\overline{V_4^{\,0}}\, P_4^{\,0} + 21\overline{V_6^{\,0}}\, P_6^{\,0}), \\ K_2 &= \frac{1}{2S}(\overline{V_2^{\,0}}\, P_2^{\,2} + \overline{V_4^{\,0}}\, P_4^{\,2} + \overline{V_6^{\,0}}\, P_6^{\,2}) \end{aligned} \tag{D.3}$$

with the Legendre polynomial $P_k^{\,m} = P_k^{\,m}(\cos\theta)$ and $\overline{V_k^{\,0}} = \overline{v_k^{\,0}} S(S-\frac{1}{2})\cdots(S-\frac{1}{2}(k-1))$. For the stable structure, the magnon energy is given by

$$\begin{aligned} \omega(\boldsymbol{q}) &= C(\boldsymbol{q}) \\ &+\sqrt{[F_1(\boldsymbol{q}) + K_1 + K_2][F_2(\boldsymbol{q}) + K_1 - K_2]}. \end{aligned} \tag{D.4}$$

By use of $K_1 = K_2$ for the helix ($\theta = \frac{\pi}{2}$), B is given by

$$S^2 B = \frac{3}{2}\overline{V_2^{\,0}} - \frac{30}{8}\overline{V_4^{\,0}} + \frac{105}{16}\overline{V_6^{\,0}} \tag{D.5}$$

Using $C(\boldsymbol{0}) = 0$, Eq. (59) and

$$K_1 - K_2 = -h\cot\theta = \frac{1}{NS\tan\theta}\frac{\partial \mathcal{E}_{cry}}{\partial\theta}, \tag{D.6}$$

we obtain the following relation

$$\lim_{\boldsymbol{q}\to\boldsymbol{0}} \omega(\boldsymbol{q}) = 0. \tag{D.7}$$

References

[1] T. Kasuya, in G. T. Rado, H. Suhl (eds.), *Magnetism IIB*, Academic Press, New York, 1966, pp. 215–294.

[2] W. C. Koehler, Magnetic Properties of Rare-Earth Metals and Alloys, *J. Appl. Phys.* **36** (1965) 1078–1087.

[3] B. R. Cooper, in F. Seits, D. Turnbull, H. Ehrenreich (eds.), *Solid State Physics* **21**, Academic Press, New York, 1968, pp. 303–400.

[4] T. Nagamiya, in F. Seits, D. Turnbull (eds.), *Solid State Physics* **20**, Academic Press, New York, 1967, 305–411.

[5] J. Jensen and A. R. Mackintosh, *Rare Earth Magnetism: Structures and Excitations*, Clarendon Press, Oxford, 1991. http://www.fys.ku.dk/ jjensen/Book/Ebook.pdf

[6] S. C. Keeton and T. L. Loucks, Electronic Structure of Rare-Earth Metals. I. Relativistic Augmented -Plane-Wave Calculations, *Phys. Rev.* **168** (1968) 672–687.

[7] W. E. Evenson and S. H. Liu, Theory of Magnetic Ordering in the Heavy Rare Earths, *Phys. Rev.* **178** (1969) 783–794.

[8] S. H. Liu, R. P. Gupta and S. K. Sinha, Generalized Susceptibility Function for Rare Earths and Thorium and Their Alloys, *Phys. Rev.* **B4** (1971) 1100–1111.

[9] P.-A. Lindgård, B. N. Harmon and A. J. Freeman, Theoretical Magnon Dispersion Curves for Gd, *Phys. Rev. Lett.* **35** (1975) 383–386.

[10] W. C. Koehler, H. R. Child, R. M. Nicklow, H. G. Smith, R. M. Moon and J. W. Cable, Spin-Wave Dispersion Relations in Gadolinium, *Phys. Rev. Lett.* **24** (1970) 16–18.

[11] P. G. Mattocks and R. C. Youg, de Haas-van Alphen effect and Fermi surface of yttrium, *J. Phys. F: Metal Phys.* **8** (1978) 1417–1467.

[12] L. W. Roeland, G. J. Cock, F. A. Muller, A. C. Moleman, K. A. McEwen, R. G. Jordan and D. W. Jones, Conduction electron polarization of gadolinium metal, *J. Phys. F: Metal Phys.* **5** (1975) L233–L237.

[13] B. N. Harmon and A. J. Freeman, Spin-polarized energy-band structure, conduction-electron polarization, spin densities, and the neutron magnetic form factor of ferromagnetic gadolinium, *Phys. Rev.* **B10** (1974) 1979–1993.

[14] R. M. Nicklow, Spin-Wave Dispersion Relation in Rare-Earth Metals, *J. Appl. Phys.* **42** (1971) 1672–1679.

[15] A. R. Mackintosh and H. Bjerrum Møller, in R. J. Elliot (ed.), *Magnetic Propertnies of Rare Earth Metals,* Plenum Press, London, 1972.

[16] P.-A. Lindgård, Spin waves in the heavy-rare-earth metals Gd, Tb, Dy, and Er, *Phys. Rev.* **B17** (1978) 2348–2360.

[17] M. S. S. Brooks, Theory of the Temperature Dependence of the Spin-Wave Excitation Energies in the Rare-Earth Metals, *Phys. Rev.* **B1** (1970) 2257–2264.

[18] N. Wakabayashi and R. M. Nicklow, Spin-wave dispersion and exchange interaction in $Y_{0.90}Tb_{0.10}$ and $Y_{0.90}Ho_{0.10}$ alloys, *Phys. Rev.* **B10** (1974) 2049–2054.

[19] N. Wakabayashi and R. M. Nicklow, in R. M. Moon (ed.) *Proceedings of the Conference on Newtron Scattering, Pt.2*, Oak Ridge National Lab., Gatlinburg, 1976, 789–792.

[20] K. Kaino and T. Kasuya, Non-linear c-f exchange interaction effect and magnetic properties of rare earth metals: I. Phase bounraries, *J. Phys. F: Metal Phys.* **11** (1981) 883–903.
[21] K. Kaino and T. Kasuya, SPIN WAVES IN RARE EARTH METALS INCLUDING NON-LINEAR s-f EXCHANGE INTERACTION EFFECT, *J. Magn. Magn. Mater.* **15–18** (1980) 1223–1224.
[22] K. Kaino and T. Kasuya, MAGNON DISPERSION IN THE CONE PHASE INCLUDING NON-LINEAR c-f EXCHANGE INTERACTION EFFECT, *J. Magn. Magn. Mater.* **31–34** (1983)169–170.
[23] K. Kaino and T. Kasuya, Non-linear c-f exchange interaction effect and mangetic properties of rare earth metals, *Research Reports of NIT, Sendai College, Hirose*, No. 45, (2015) 1–16.
https://www.jstage.jst.go.jp/article/nitsendaih/45/0/45_1/_pdf
[24] B. N. Harmon and A. J. Freeman, Augmented-plane-wave calculation of indirect-exchange matrix elements for gadolinium, *Phys. Rev.* **B10** (1974) 4849–4855.
[25] S. Tomonaga, Remarks on Bloch's Method of Sound Waves applied to Many-Fermion Problems, *Prog. Theor. Phys.* **5** (1950) 544–569.
[26] T. Holstein and H. Primakoff, Field Dependence of the Intrinsic Domain Magnetization of a Ferromagnet, *Phys. Rev.* **58** (1940) 1098–1113.
[27] P. W. Anderson, *Concepts in Solids,* Benjamin, New York, 1963, pp. 164–182.
[28] N. N. Bogolyubov and S. V. Tyablikov, Retarded and Advanced Green Functions in Statistical Physics, *Soviet Physics Doklady* **4** (1959) 589–593.
[29] Y. Nagaoka, Dynamical Theory of Spin Waves in Ferromagnetic Metals with s-d Exchange Interaction, *Prog. Theor. Phys. Kyoto* **28** (1962) 1033–1047.
[30] R. A. Tahir-Kheli and D. ter Haar, Use of Green Functions in the Theory of Ferromagnetism. I. General Discussion of Spin-S Case, *Phys. Rev.* **127** (1962) 88–94.
[31] J. W. Cable and W. C. Koehler, A neutron study of the spin reorientation transition in Gd, *J. Appl. Phys.* **53** (1982) 1904–1906.
[32] A. Narita and T. Kasuya, EFFECTS OF BAND STRUCTURE AND MATRIX ELEMENT ON RKKY INTERACTION, *J. Magn. Magn. Mater.* **43** (1984) 21–42.
[33] W. C. Koehler, J. W. Cable, M. K. Wilkinson and E. O. Wollan, Magnetic Structures of Holmium. I. The Virgin State, *Phys. Rev.* **151** (1966) 414–424.
[34] W. C. Koehler, in R. J. Elliot (ed.), *Magnetic Properties of Rare Earth Metals*, Plenum Press, London, 1972.
[35] H. R. Child, W. C. Koehler, E. O. Wollan and J. W. Cable, Magnetic Properties of Heavy Rare Earths Diluted by Yttrium and Lutetium, *Phys. Rev.* **138** (1965) A16554–A16560.
[36] T. M. Holden, B. M. Powell, M. W. Stringfellow and A. D. B. Woods, Spin-Wave Excitation in $Ho_{0.5}Er_{0.5}$, *J. Appl. Phys.* **41** (1970) 1176–1177.
[37] R. M. Nicklow, N. Wakabayashi, M. K. Wilkinson and R. E. Reed, Spin-Wave Dispersion Relation for Er Metal at 4.5°K, *Phys. Rev. Lett.* **27** (1971) 334–337.
[38] P.-A. Lindgård and O. Danielsen, Bose-operation expansion of tensor operators in the theory of magnetism, *J. Phys. C: Solid State Phys.* **7** (1974) 1523–1535.